Pre-chamber ignition systems for high-speed large-bore gas engine: technology investigation through 3D-CFD analysis

Fuel 411 (2026) 138004

Contents lists available at ScienceDirect

Fuel

journal homepage: www.elsevier.com/locate/fuel

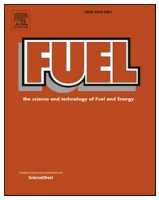

Full Length Article

Pre-chamber ignition systems for high-speed large-bore gas engine: technology investigation through 3D-CFD analysis

Federico Millo [a], Massimiliano Zanatta [a], Andrea Scalambro [a], Andrea Piano [a,*], Francesco Accurso [b], Francesco C. Pesce [b], Alberto L. Vassallo [b]

[a] Politecnico di Torino, Energy Department (DENERG), Corso Duca degli Abruzzi, 24, 10129 Torino, Italy
[b] Dumarey Automotive Italia S.p.A., Corso Castelfidardo, 36, 10129 Torino, Italy

ARTICLE INFO

Keywords:
Methane
Large-bore
Pre-chamber ignition systems
Advanced combustion systems

ABSTRACT

Nowadays large bore gas engines are gaining popularity in the market for power generation and marine applications. Methane is preferred over conventional diesel because of its favourable H/C ratio and lower soot emissions. Furthermore, the global transition to renewable energy sees eMethane as one of the most promising options for clean energy storage. Consequently, the enhancement of the efficiency of large bore gas engines through innovative combustion strategies, such as pre-chamber ignition, is of growing importance. This technology increases ignition energy, shortens combustion duration, and achieves higher thermal efficiency compared with conventional ignition systems due to extended lean operation. However, it remains unclear which factors fundamentally limit the achievable lean operation of passive and active pre-chamber ignition systems, thereby influencing their combustion behaviour and pollutant emission.

In this context, this paper presents a 3D-CFD numerical investigation of a large bore gas engine (~4 L/cyl.) equipped with both passive and active pre-chamber systems, operating under lean air/methane mixtures at high load. The study aims to evaluate the influence of calibration and geometric parameters, define and optimize the lean limit of each system, and assess the resulting impact on engine thermal efficiency and pollutant emissions.

A comprehensive comparison between the two systems is provided. Finally, the results of the optimization process demonstrate that both passive and active pre-chamber systems can be effectively tailored through geometry and calibration to address the dual challenge of high efficiency and low NO_x emissions in large bore methane engines.

1. Introduction

The decarbonization of the global transportation and energy sectors has placed increasing pressure on large bore internal combustion engines (ICEs), particularly those used in marine propulsion and stationary power generation. To reduce greenhouse gas (GHG) emissions and align with international climate goals, these engines have been undergoing a progressive shift from traditional diesel fuel to lower-carbon alternatives or non-fossil fuels. This transition includes the adoption of natural gas (NG), biomethane, and other renewable gaseous fuels, which offer a significantly lower carbon intensity compared to conventional marine diesel oil [1]. In parallel, increasingly stringent regulations have been introduced to limit the local pollutant emissions associated with combustion processes. In particular, the International Maritime Organization (IMO) has introduced Tier III Nitric Oxides (NO_x) emission standards under MARPOL Annex VI [2], requiring up to 80 % NO_x reduction compared to Tier I levels for engines operating in Emission Control Areas [3]. In this context, gas engines have emerged as a promising solution for the maritime sector. Natural gas offers a cleaner alternative to traditional marine fuels, providing lower CO_2 and NOx emissions [4]. The transition to gas-powered engines is expected to accelerate over the next few years, driven by both regulatory pressures and the maritime industry's commitment to sustainability [5]. According to the International Energy Agency (IEA), natural gas consumption in the marine sector is projected to increase steadily, making Liquified Natural Gas (LNG) a preferred fuel due to its cleaner-burning properties [6]. However, achieving ultra-low NO_x emissions without relying on exhaust aftertreatment systems (e.g., Selective Catalytic Reduction, SCR) remains a major technological challenge. Conventional lean-burn spark-ignition (SI) strategies, while effective in reducing peak temperatures and thus NO_x formation, often suffer from unstable ignition, slow

* Corresponding author.
E-mail address: andrea.piano@polito.it (A. Piano).

https://doi.org/10.1016/j.fuel.2025.138004
Received 25 September 2025; Received in revised form 28 November 2025; Accepted 10 December 2025
Available online 17 December 2025

Nomenclature

AMR	Adaptive Mesh Refinement
A_{NOZZLE}	Outlet nozzle area
aPC	Active pre-chamber
aTDCf	after TDC firing
BMEP	Brake Mean Effective Pressure
BSL. Geom.	Baseline geometry
bCJE	before Cold Jet Ejection
bTDCf	before TDC firing
CAD	Crank Angle Degree
CFD	Computational Fluid Dynamics
CI	Compression Ignition
CJE	Cold Jet Ejection
CJL	Cold Jet Losses
CoV	Cycle-to-cycle Variability
CR	Compression Ratio
Da	Damköhler number
DI	Direct Injection
DNS	Direct Numerical Simulation
EATS	Exhaust Aftertreatment System
EGR	Exhaust Gas Recirculation
EoE	End of Ejection
FP	Fuel Power
GHG	Greenhouse gas
HJE	Hot Jet Ejection
HR aHJE	Heat Release after HJE
HR bHJE	Heat Release before HJE
HR dHJE	Heat Release during HJE
HRR	Heat Release Rate
HL	Heat Losses
ICE	Internal Combustion Engine
ID	Ignition Delay
IEA	International Energy Agency
IMEP	Indicated Mean Effective Pressure
IMO	International Maritime Organization
ISHC	Specific unburned hydrocarbons emissions
ISNOx	Specific NOx emissions
ITE	Indicated Thermal Efficiency
Ka	Karlovitz number
LES	Large Eddy simulation
LFS	Laminar Flame Speed
L_f	Laminar flame thickness
L_i	Integral lenght scale
LNG	Liquefied Natural Gas
MC	Main Chamber
MFB10-75	Combustion duration in CAD from 10 % to 75 % Mass Fraction Burned
MFB50	Crank angle at 50 % Mass Fraction Burned
MN	Methane Number
NG	Natural Gas
NOx	Nitric Oxides
OPT. Geom.	Optimized Geom.
PC	Pre-chamber
PFI	Port-fuel Injection
PFP	Peak Firing Pressure
pPC	Passive pre-chamber
RANS	Reynolds-Averaged Navier-Stokes
RCEM	Rapid Compression Expansion Machine
RCM	Rapid Compression Machine
SCE	Single-cylinder Engine
SCR	Selective Catalytic Reduction
SI	Spark-ignition
S_L	Laminar flame speed
SOI	Start of Injection
ST	Spark timing
TA Luft	*Technische Anleitung zur Reinhaltung der Luft*/Technical Instructions on Air Quality Control
TCI	Turbulence Chemistry Interaction
TDC	Top Dead Center
TDCf	Top Dead Center firing
TJI	Turbulent Jet Ignition
TKE	Turbulent Kinetic Energy
u'	Turbulent velocity
uHC	Unburned Hydrocarbons
V_{PC}	Pre-chaber volume
WSR	Well-Stirred Reactor
γ	Specific heat ratio
Δp_{PC-MC}	Pressure difference between PC and MC
λ	Relative air-to-fuel ratio
Φ	Equivalence Ratio

flame development, and limited combustion efficiency under lean conditions.

Pre-Chamber (PC) ignition has emerged as a promising approach to overcome these limitations [7]. In a PC system, combustion is initiated in a small volume, either passive or active, that communicates with the main chamber (MC) through a set of calibrated orifices. As the flame develops inside the pre-chamber, high-temperature reactive jets are expelled into the main chamber, triggering multi-point ignition and promoting fast flame propagation. The larger ignition volume in the main chamber is less affected by lean spots given by poor mixing. As a consequence, cycle-to-cycle combustion variation is improved, and it is possible to ignite leaner overall mixtures [8]. The SI lean-burn combustion concept is generally associated with improved engine efficiency and decreased NOx emissions. As explained in detail by Toulson et al. [9], in their comprehensive review of PC systems up to 2010, the addition of air leads to an increase in efficiency due to an increased specific heat ratio (γ), a reduction of pumping losses by tending towards throttle-less operation, and a reduction in wall heat losses caused by lower temperatures. Flame temperatures are reduced as the air–fuel mixture becomes leaner [10] and Warnatz, et al. [11] observed almost insignificant NOx emissions generated by Zeldovich mechanism below 1800 K.

In a passive pre-chamber (pPC), the mixture is drawn in naturally from the main chamber during compression, whereas an active pre-chamber (aPC) incorporates separate fuel injection to enrich the mixture and enhance jets energy. Studies by Yang et al. [12] and Shah [13] have shown that aPC systems provide better control over the local equivalence ratio, jet symmetry, and ignition stability, especially under highly diluted conditions. Conversely, pPC offers simplicity and retrofit compatibility but can suffer from higher cyclic variability and weaker jet penetration.

A broad range of experimental campaigns has validated the effectiveness of pre-chamber ignition systems in enabling ultra-lean combustion and reducing NO_x emissions in large bore NG engines. These studies span from optically accessible rapid compression machines (RCMs), in order to better understand the main principles of the combustion process, to full-scale single-cylinder engine test benches with the goal of assessing the real potential of these systems.

In optically accessible RCMs, researchers have visualized jet ignition dynamics using high-speed OH*/CH* chemiluminescence imaging. Gentz et al. [14] demonstrated that number and diameter of orifices are critical parameters in the effectiveness of the combustion, and the

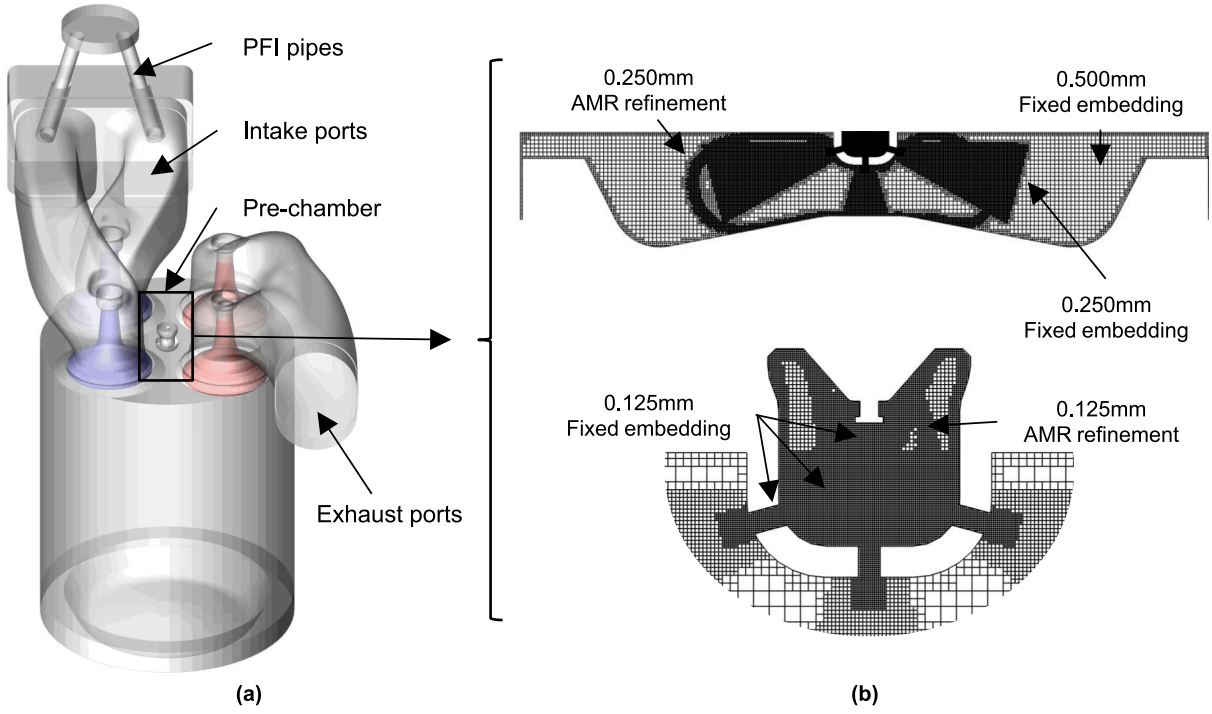

Fig. 1. a) Schematic view of the 3D numerical domain. b) grid details for main chamber and pre-chamber.

optimal configuration depends on the actual operating conditions and the excess air quantity. During their research activity, they discovered that for close-to-stoichiometric conditions, higher-diameter orifices generate jets that are volumetrically distributed throughout the main chamber and improve the consumption of the charge. Nevertheless, for leaner conditions, smaller diameter orifices are required to produce narrow, high-velocity jets to initiate combustion. Similarly, Li et al. [15] found that the ratio of outlet nozzle area to pre-chamber volume (A_{nozzle}/V_{PC}) is the key structure parameter of pre-chamber systems to determine the ignition mode of the main chamber. Shapiro et al. [16] conducted a parametric study on multiple pre-chamber geometries using a Rapid Compression Expansion Machine (RCEM), quantifying the influence of volume and tangential nozzle angle. In that study, the emerging favourable design consisted of straight nozzles and larger volume in order to deliver better mixing, more rapid combustion and higher energy flame jets. Taking into account that these studies cannot precisely reproduce the high turbulence of a combustion chamber and the essential interaction between piston shape and pre-chamber, all the insights emerging from these studies have directly informed the pre-chamber design and optimization strategies pursued in this work, as discussed later in Section5.

Engine test bench experiments have provided robust evidence of the effectiveness of PC ignition systems under ultra-lean conditions in large-bore NG engines. Lu et al. [17] evaluated a pPC system in a 12.9 L 6-cylinder natural gas engine under part-load conditions and demonstrated that NO_x emissions below IMO Tier III limits could be achieved with a relative air-to-fuel ratio (λ) equal to 1.9 (achieved NOx emissions = 0.34 g/kWh), without the use of any aftertreatment system. However, they also reported that increased lean dilution led to a rise in cycle-to-cycle variability (CoV) and elevated unburned methane (CH_4) emissions. At higher load operation, Eicheldinger et al. [18] conducted an experimental campaign on a ~5L NG single-cylinder engine (SCE), operating both passive and active PC configurations at Brake Mean Effective Pressure (BMEP) levels above 30 bar. The passive system was found to maintain stable combustion up to $\lambda \approx 1.8$, with NO_x emissions below the threshold of 500 mg/m^3 imposed by the German regulation entity for the control of the atmospheric pollution (TA-Luft [19,20]). Concerning the aPC concept, they claimed that the higher energy inside the pre-chamber allows to ignite significantly leaner MC mixtures. Nevertheless, tests were reported up to $\lambda_{MC} = 1.85$. On the other hand, Shah et al. [21] experimentally found on a 2L SCE that aPC lean limit was at $\lambda_{MC} = 2.9$, showing a significant extension with previously found results with pPC at $\lambda_{MC} = 1.7$ [22]. More recently, Yang et al. [12] proposed a detailed comparison between the combustion process of the two systems equipped on 6L SCE carried out at medium load (10–12 bar Indicated Mean Effective Pressure – IMEP), showing reduced NO_x emissions for aPC at $\lambda_{MC} = 2.0$ and pPC at $\lambda_{MC} = 1.5$. In this case, there are no mentions related to the lean limits of the two systems. These findings validate the potential of PC ignition as a viable strategy for achieving high efficiency and ultra-low emissions in large-bore NG engines.

Given the early-stage nature of this development, and in the absence of experimental data in the initial phases, 3D-CFD modeling played a fundamental role in building a first-principles understanding of the pre-chamber ignition system. This approach enabled the exploration of fundamental combustion characteristics, limitations, and operational boundaries of both passive and active PC configurations under realistic large bore conditions. The insights obtained from these numerical investigations supported the design of different gas combustion systems, the selection of the most appropriate pre-chamber geometries and the proper integration in the engine. Preliminary results of the experimental campaign are reported in [23,24].

Three-dimensional CFD is widely employed in the development of pre-chamber combustion systems, especially to support the design and optimization of pre-chamber geometry. For instance, Jeong et al. [25] used CFD to evaluate the influence of nozzle layout on jet structure and combustion performance in a 12L/cyl. NG engine.

However, accurately simulating the interaction between the pre-chamber and main chamber remains challenging, and multiple modeling strategies have been proposed. For turbulence modeling, Reynolds-averaged Navier-Stokes (RANS) approach has been widely adopted in literature [26,27] to gather useful insights that cannot be experimentally studied, significantly reducing the computational time with respect to turbulence-resolving approaches such as Large Eddy Simulation (LES) or Direct Numerical Simulation (DNS). Focusing on the

Table 1
Natural Gas Large bore engine platform specifications.

Bore [mm]	170
Stroke [mm]	185
Displacement Volume [dm^3]	4.2
CR [-]	11
Number of Valves	2-intake 2-exhaust
Injection system	PFI (+DI aPC)

combustion model, simplified approaches like the G-equation model were considered by Xu et al. [28] and Kim et al. [29], assessing its limitations with extreme lean mixtures. Piano et al. [30] demonstrated that PC ignition combustion spans multiple regimes with a lean pre-chamber fueled with gasoline and concluded that no single model can accurately capture all relevant phenomena. Nevertheless, in that study the SAGE combustion model was chosen to track the chemical species throughout the combustion process.

Despite these advancements, the literature still lacks systematic comparative studies between passive and active pre-chamber ignition systems under full load operating conditions representative of large bore, high-speed engines for marine and stationary applications. In particular, a coherent comparison of the two architectures operated near their respective lean limits is missing, and it therefore remains unclear which engine features fundamentally dictate these limits. In this work, the combustion process of both systems is analysed in detail, with specific attention to the phenomena that restrict their operation toward more diluted mixtures and higher indicated thermal efficiency.

Moreover, the available literature does not clearly describe the relative contribution of the pre-chamber and main chamber to the NOx formation process. In this study, extensive effort has been devoted to characterising the origin of NOx emissions for both systems. Addressing these knowledge gaps and understanding the key limitations and potential of PC systems is critical to supporting the development of a robust, scalable combustion platform for IMO Tier III-compliant large bore marine and stationary engines.

2. Engine test case

Numerical experiments were performed on the large bore engine platform designed by DUMAREY. This platform is specifically designed for high-speed (engine speed >1000 rpm), large bore engines and consists of a turbocharged single cylinder, featuring a bore diameter of 170 mm and a stroke length of 185 mm. For this application, in which natural gas has been chosen as fuel, the compression ratio (CR) has been set equal to 11:0. Considering the relevance of retrofit-ability of diesel engines, only minimal and necessary modifications have been implemented on the reference diesel-fuelled platform. In this extent, the intake ports have been re-designed in order to reduce the induced swirl motion, typical of compression ignition (CI) concepts, while introducing a certain tumble level beneficial for improving turbulence and therefore flame speed. The piston is characterized by a light omega-shape open design, as a good compromise to accommodate both passive and active pre-chamber combustion processes, as shown in Fig. 1. The main characteristics of the engine test case are reported in Table 1.

Two different designs for each combustion concept have been analyzed, a baseline and an optimized one. The selected baseline passive pre-chamber design is characterized by radial holes and 1 axial hole that has been proven to be beneficial to improve engine performance, especially at very lean conditions [31], thanks to improved scavenging [32] and increased Turbulent Kinetic Energy (TKE) around the spark plug. The major difference between the baseline and optimized pPC is in the holes number, dimensions and orientation. In particular, 6 tilted holes, which provide a swirl motion to the inflow charge, are adopted in the optimized pPC configuration. As far as the active pre-chamber concept is concerned, it is characterized by 6 radial holes, and higher internal volume in comparison to passive design. In this case, the optimization involves a reduction of the internal volume together with a significant decrease in hole diameter, resulting in a ~20 % reduction of the nozzle area–volume ratio (A_{nozzle}/V_{PC}). Dimensions of both systems are aligned with those of external manufacturers as synthetically reported by Shah et al. in [33]. In summary, the characteristics of the different pre-chamber designs are reported in Table 2.

Table 2
Passive and active pre-chambers specifications.

	pPC baseline	pPC optimized	aPC baseline	aPC optimized
Radial Holes [#]	4	6	6	6
Axial Holes [#]	1	1	–	–
Orientation	Radial	Swirling	Radial	Radial
Inclination [deg]	17	17	20	17
V_{PC}/V_{TDC} [%]	<0.5	<0.5	<1.5	<0.8
Nozzle size	REF	REF − 15 %	REF + 40 %	REF − 6 %
A_{nozzle}/V_{PC} [cm^{-1}]	0.061	0.062	0.031	0.025

Table 3
Summary of the engine parameters adopted during the numerical investigation.

	pPC	aPC
Engine Speed [rpm]	1500	
Target BMEP [bar]	23	
Intake pressure [bar]	3.2–3.6	3.4–4.2
PFI injection [CAD aTDCf]	−360	
PFI injection flow rate [g/s]	70	
DI injection – aPC [CAD aTDCf]	–	−180
DI injection flow rate [g/s]	–	2
Main chamber relative air-to-fuel ratio (λ_{MC})	1.7–1.9	1.8–2.2

Table 4
Main settings of the developed 3D-CFD CONVERGE model.

Turbulence model	RANS RNG k-ε	
Heat transfer model	O'Rourke and Amsden	
Combustion model	SAGE	
Kinetic mechanism	San Diego 2016 [36]	
Spark energy [mJ]	pPC = 200	aPC = 40
Base grid size [mm]	8	
Minimum grid size [mm]	MC = 0.250	PC = 0.125

In the end, the two pre-chamber concepts differ in the spark plug adopted, since, as reported in literature [34], pPC for large bore gas applications requires dedicated spark plugs characterized by higher ignition energy in comparison with aPC concept, since this latter usually ignites richer, and thus more reactive mixtures, inside the PC.

For both concepts, the Port-Fuel (PFI) start of injection (SOI) in the gas pipes is phased at top-dead-center (TDC) with the intake valves already opened. Injection pressure has been controlled in order to get a fixed pressure difference with the intake ambient, resulting in an almost constant PFI mass flow rate of 70 g/s at full load operation. Hence, the injection duration has been calibrated in order to run the numerical campaign with fixed total mass of injected fuel. The direct injection (DI) for the active concept started at 180 CAD bTDCf and is characterized by fixed flow rate of 2 g/s. The amount of directly injected fuel is considered within the total fuel mass computation. The dilution ratio has been controlled by adjusting the boost pressure. More detailed indications on the working points explored in this study are available in Table 3. The injected fuel consisted of a non-derated methane quality commonly available at gas station, characterized by a methane number (MN) of 84.

3. Numerical model

The 3D numerical domain, representing the large bore engine platform, includes the intake plenum, intake ports, main chamber, pre-

Table 5
Engine relevant conditions analysed for the 0D and 1D calculations for ignition delay and laminar flame speed assessments.

		Ignition delay			Laminar flame speed		
		Min	Max	Step	Min	Max	Step
Temperature	[K]	800	1200	100	600	1000	100
Pressure	[bar]	50	170	20	30	130	20
Φ	[–]	0.5	1.1	0.05	0.5	1.1	0.05
EGR ratio	[–]	0	0.2	0.05	0	0.2	0.05

chamber and exhaust ports (see Fig. 1). Numerical experiments have been carried out on CONVERGE CFD software v3.0.25 [35].

The main setup parameters of the model are listed in Table 4.

RANS approach coupled with RNG k-ε model was adopted for turbulence modelling [37], which is a common choice due to its ability to account for fundamental physical aspects of flame propagation, such as compressibility effects and strongly rotating vortices (e.g. suitable for swirling PC). Wall heat transfer was modelled according to the formulation by O'Rourke and Amsden [38] using a von Karman constant of 0.42. The simulations employed the Redlich–Kwong equation of state. Real gas properties were defined as temperature-dependent, and mixture-averaged diffusion was assumed. Global transport parameters were set to 0.9 for Prandtl number and 0.78 for Schmidt number, following the 3D setup of [39]. The injection events (both PFI and DI) have been modelled with imposed mass-flow rate of a methane surrogate through inlet boundaries. In order to replicate the behaviour of the fuel mentioned in Section 2, a methane surrogate with a calculated MN of 84 (from Wartsila online MN calculator [40]) has been chosen for this numerical campaign.

Total pressure and temperature were set at the inlet, while static pressure and temperature were imposed at the outlet of the exhaust ports. Initial conditions, including temperature and pressure above-mentioned, injection flow rates, and species concentrations, were extracted from the correlated 1D-CFD SCE model developed in GT-SUITE environment [41].

Due to the absence of experimental data, SAGE combustion model was utilized for the simulations. The SAGE model is well-suited for representing Turbulent Jet Ignition (TJI) processes due to its capability to accurately simulate flame front propagation and chemical reactions under varying turbulence levels. Piano et al. [30] have demonstrated the effectiveness of the SAGE model in representing TJI ignition through detailed analysis of the Damköhler number (*Da*) on the flame front. For a reliable and predictive simulation campaign, the selection of the reaction mechanism was essential. Thus, an extensive literature review has been carried out, looking at the most robust kinetic mechanisms for these applications. Zhang et al. conducted comprehensive studies comparing results from available mechanisms with a wide set of experimental data including shock tube and rapid compression machine measurements [42] as well as laminar burning velocity experiments [43].

Among all the mechanisms tested by Zhang, only three mechanisms were considered: the AramcoMech2.0 (2016) [44–47] (species 493, reactions 2716), as the most reliable predictive mechanism characterized by the lower combined error in terms of both ignition delay and laminar flame speed; the San Diego mechanism (2016) (species 58, reactions 270) [36] was considered due to its low combined error, reduced number of species and reactions. The third considered mechanism was GRI-Mech 3.0 (2000) (species 53, reactions 325) [48] since it is a widely adopted kinetic mechanism in the literature for similar applications [12,25,27,49]. Taking into account that chemistry computational time increases quadratically with the number of species and linearly with the number of reactions [35], AramcoMech2.0 was considered as not suitable for the 3D-CFD analysis campaign. Nevertheless, it was used as reference mechanism for comparing the results of the other two mechanisms in terms of ignition delay and laminar flame speed through 0D and 1D chemistry simulations. Table 5 summarizes the engine relevant conditions in which the three kinetic mechanisms were tested through the 0D and 1D chemistry numerical assessment.

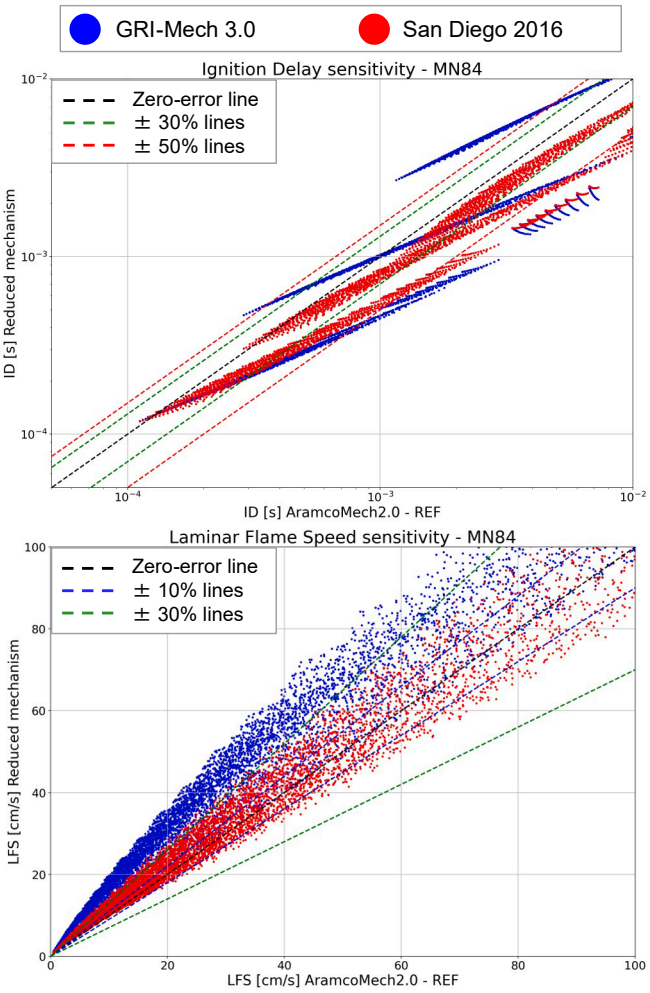

Fig. 2. Ignition delay (top) and laminar flame speed (bottom) correlation plots. X-axis represents the reference mechanism (AramcoMech2.0), Y-axis represents tested mechanisms, blue for GRI-Mech 3.0, red for San Diego 2016. (For interpretation of the references to colour in this figure legend, the reader is referred to the web version of this article.)

Results are expressed through correlation plots shown in Fig. 2, in which both GRI-Mech 3.0 (blue dots) and San Diego 2016 (red dots) are compared with the reference AramcoMech2.0 for both ignition delay (top) and laminar flame speed (bottom). Starting from ignition delay (ID), it is evident by the correlation plot on the top of Fig. 2 that San Diego 2016 (red dots) stands mainly between the zero and −30 % error lines, meaning a limited and consistent underestimation of ignition delay time. On the other hand, GRI-Mech3.0 showed differences with respect to AramcoMech2.0, ranging from ±50 %. Results in terms of Laminar flame speed (LFS) showed an overall better predictivity with San Diego 2016, confirming the results related to ignition delay prediction. For these reasons, San Diego 2016 has been finally selected for the numerical analysis carried out in this study.

Different sensitivity analyses have been carried out to understand the impact of grid settings on the evolution of the combustion process. It has been found that results of simulations are highly influenced by the number of cells in the pre-chamber holes. In accordance with other studies [39,50], nozzles were discretized with a minimum cell size of 0.125 mm, as the best compromise between reliability of the results and computational cost. Moreover, further refinements were introduced in

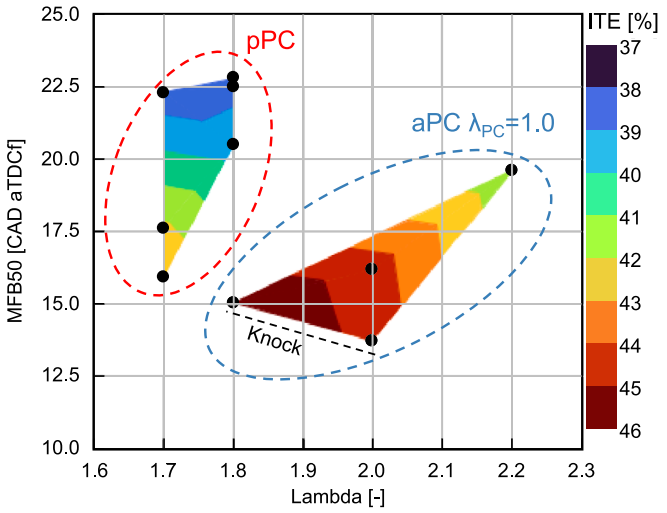

Fig. 3. ITE contour map for passive (pPC) and active (aPC) pre-chamber concepts.

the bottom part of the pre-chamber and at the outlet of the holes in the main chamber to properly describe the jet/flame exiting phase. In both the passive and active concepts, a spherical fixed embedding has been used to reduce the grid size in proximity of the spark plug up to the minimum grid size. Moreover, Adaptive Mesh Refinement (AMR) technique was used to locally refine the computational grid, based on the local gradients of velocity and temperature. AMR can refine both MC and PC up to their minimum grid size. A schematic representation of the grid settings used in the pre-chamber region is shown in Fig. 1. Spark plug has been modelled through two consecutive energy sources to replicate the breakdown and the arc-and-glow phases.

4. Results: combustion comparative analysis

The main goal of this research activity was to characterize the two combustion concepts, and to understand their limitations and potentialities. An initial assessment has been carried out evaluating the indicated thermal efficiency (ITE) achieved by the two systems at λ_{MC} values > 1.7. The choice of the lean working region is derived by the practical goal of this study, which aims to sustain the development of a large bore platform compliant with NOx IMO Tier III restrictions without any dedicated exhaust after-treatment system (EATS) [23].

Fig. 3 shows the ITE for the pPC and the aPC systems in a λ- MFB50 plane, in which each simulation is represented by a black dot. The x-axis represents the global λ value in the main chamber, while the y-axis reports the anchor angle MFB50. The MFB50 was preferred to the Spark Timing (ST), as suggested by [18].

Two clouds of points are shown, the left one representing the passive pre-chamber concept, while the other represents the active pre-chamber one, running with the overall λ value in pre-chamber close to stochiometric. In both concepts, higher efficiency is achieved for an advanced combustion anchor angle. With the passive pre-chamber concept, the increased mixture dilution (i.e., $\lambda_{MC} \geq 1.8$) does not allow a proper phasing of combustion, even when advancing the spark timing, as highlighted by the MFB50 which remains higher than 20 CAD aTDCf. The increased combustion duration, indeed, cannot be counteracted by advanced spark timings (>30 CAD bTDCf) because of the poor scavenging of the pre-chamber which leads to a slow flame propagation in

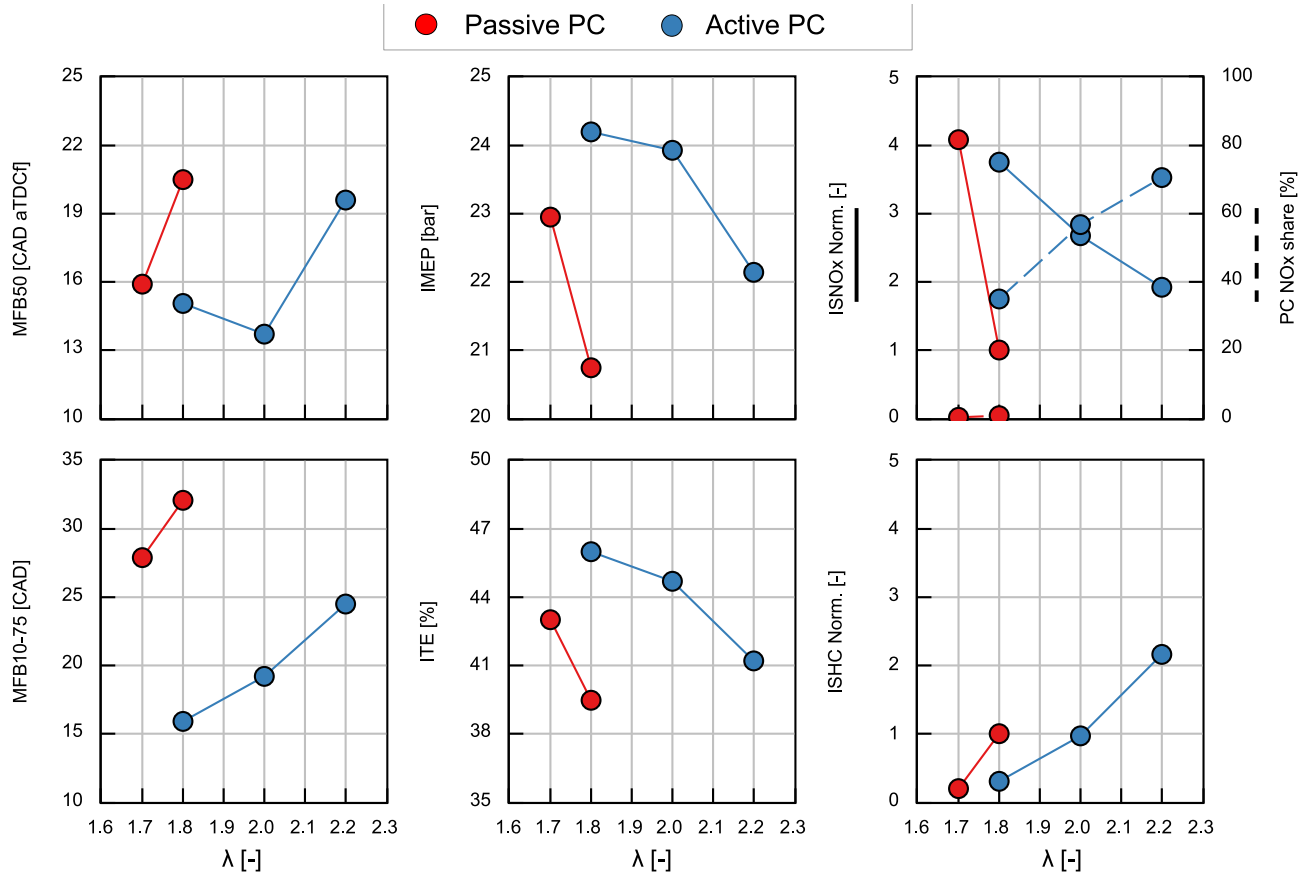

Fig. 4. Results in terms of combustion indicators (MFB50. MFB1075, IMEP, ITE) and normalized specific emissions (ISNOx, ISHC) for pPC and aPC concepts. Emissions have been normalized with respect to results obtained with pPC concept at λMC = 1.8.

PC, finally lowering the energy of the turbulent jets exiting from the pre-chamber nozzles. On the other hand, in the active pre-chamber concept, it is possible to actively control the amount and the rate at which energy is released in the pre-chamber thanks to the fuelling of the pre-chamber itself, thus allowing the extension of the lean limit with proper combustion phasing. Nevertheless, the increased combustion duration at λ values >2.0 leads to a reduction in the efficiency. With both the pre-chamber systems, MFB50 values lower than 14 CAD aTDCf were not achievable due to knock occurrence, in agreement with [51], where typical anchor angles for similar applications were experimentally found to be higher than the typical 8–10 CAD aTDCf [52].

In order to provide a more comprehensive understanding of the previously described results, Fig. 4 summarizes the combustion indicators (MFB50, MFB10-75), performance indicators (IMEP, ITE) and specific emissions of NOx and unburned hydrocarbons (ISNOx,ISHC) for both concepts (red for the pPC, blue for aPC) considering the optimal combustion phasing for each mixture composition. As previously mentioned, it was not possible to achieve MFB50 values lower than 20 CAD aTDCf with the pPC concept for λ higher than 1.8. On the contrary, earlier centres of combustion can be achieved with the aPC concept even at λ_{MC} higher than 2.0. The major difference between the two concepts lies in the combustion duration (MFB 10–75) that is drastically and consistently lower with the aPC concept due to the higher ignition energy conveyed by the jets. This is reflected in performance indicator results, where aPC concept gets higher efficiency for the combinations of two reasons: more advanced MFB50 and leaner mixture [9]. Specific emissions are normalized with respect to pPC $\lambda_{MC} = 1.8$. Looking at NOx emissions, compared with the aPC concept, the pPC shows reduced levels of emissions at equal λ_{MC} value. This is due to the lower temperatures in MC, which mitigates the thermal NOx formation process ([53,54]), and the different mixture composition in the pre-chamber. In the passive configuration, the pre-chamber operates with higher λ_{PC} values, as its entire fuelling is provided by the already lean mixture drawn from the main chamber ($\lambda_{PC} \sim \lambda_{MC}$). As a result, NOx formation within the pre-chamber proceeds at a rate comparable to that in the MC, and the share of PC-generated NOx emissions remains comparable to the PC/MC fuel trapped energy ratio (~0.5 %), as shown by the dashed lines in Fig. 4. The global NOx emissions predicted for the passive concept were also validated against the experimental data available in [24], confirming that the model correctly captures the NOx emission levels for highly diluted methane combustion. However, due to technical constraints, experimental validation of the PC/MC NOx split was not possible. The active pre-chamber exhibits fundamentally different characteristics. Here, the pre-chamber operates with a nearly stoichiometric mixture ($\lambda_{PC} \sim 1.0$), whereas the main chamber mixture is substantially leaner ($\lambda_{MC} > 1.8$). Under these conditions, the pre-chamber reaches significantly higher temperatures and pressures, which strongly enhance thermal-NOx formation, while the main chamber operates in a regime where NOx formation in CH_4–air flames is known to be very limited. In this operating mode, the simulations performed in the present study show that up to 70 % of the total NOx emissions are formed inside the pre-chamber for the baseline aPC. These results are fully consistent with the trends reported by Accurso et al. [55] for a large-bore natural-gas engine equipped with an active pre-chamber, where the PC contribution to NOx exceeded 80 % under high-boost operation. Importantly, in [55] was shown that the PC-NOx share increases with boost pressure, as the main-chamber mixture becomes progressively leaner and its contribution to NOx becomes negligible. A similar trend is reproduced in the present study. As shown in Fig. 4, increasing λ_{MC} leads to an overall reduction of NOx due to the lower MC contribution, while the NOx formed inside the pre-chamber remains nearly unchanged because $\lambda_{PC} \sim 1.0$ is kept constant. Consequently, the PC/MC NOx ratio increases as λ_{MC} increases. It is important to stress that the primary objective of this numerical investigation is to identify and understand the NOx formation trends, which are essential for guiding pre-chamber geometry optimization in large-bore natural-gas engines.

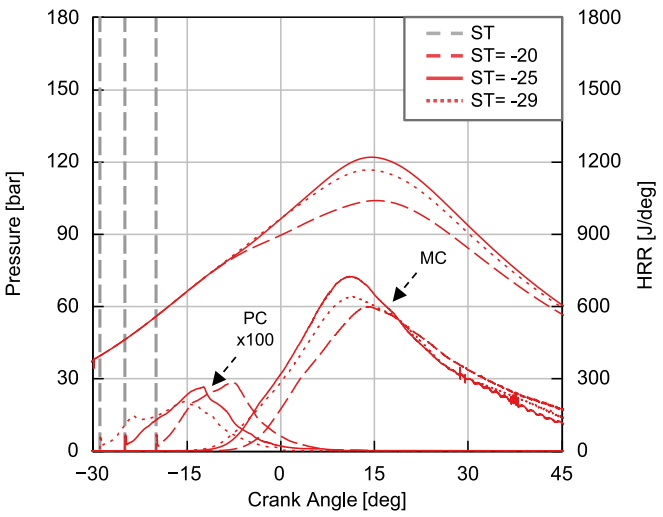

Fig. 5. Pressure and HRR traces for a spark timing sweep with pPC @ λ = 1.7.

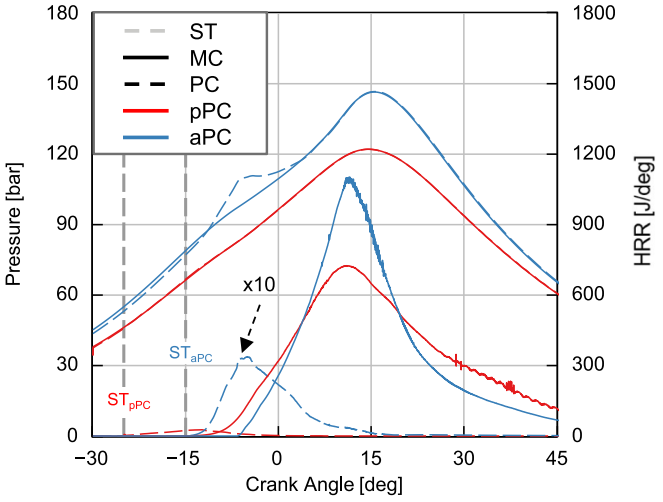

Fig. 6. Comparison in terms of pressure and HRR profiles between pPC @ λMC = 1.7 in red, aPC @ λMC = 2.0, λPC = 1.0 in blue. (For interpretation of the references to colour in this figure legend, the reader is referred to the web version of this article.)

These insights directly supported the design choices presented in Section 5. Eventually, unburned hydrocarbons (HCs) increase for increased air dilution and as expected, the aPC concept leads to a global reduction of HC thanks to improved combustion phasing and combustion duration.

As abovementioned, the combustion phasing of the pPC concept cannot be optimized by simply acting on the spark timing, thus resulting in a minimum MFB50 close to 15 CAD. To better highlight the reasons behind this behaviour, Fig. 5 shows a spark timing sweep performed with the baseline pPC at $\lambda_{MC} = 1.7$. As can be seen, the highest peak firing pressure (PFP) and the shortest combustion process has been achieved with ST = −25 CAD aTDCf, while further ST advance was not able to anticipate combustion towards the TDCf. Focusing on the pre-chamber heat release rate (HRR) (dashed lines), it is possible to notice that combustion intensity inside the pre-chamber reduces for more advanced spark timings; therefore, also the ignition energy associated with the hot and turbulent jets issuing from the pre-chamber nozzles decreases. This is due to multiple combined effects: reduced fuel filling, less convenient thermodynamic conditions and poor scavenging of the pre-chamber.

Going deeper into the comparison between the combustion process

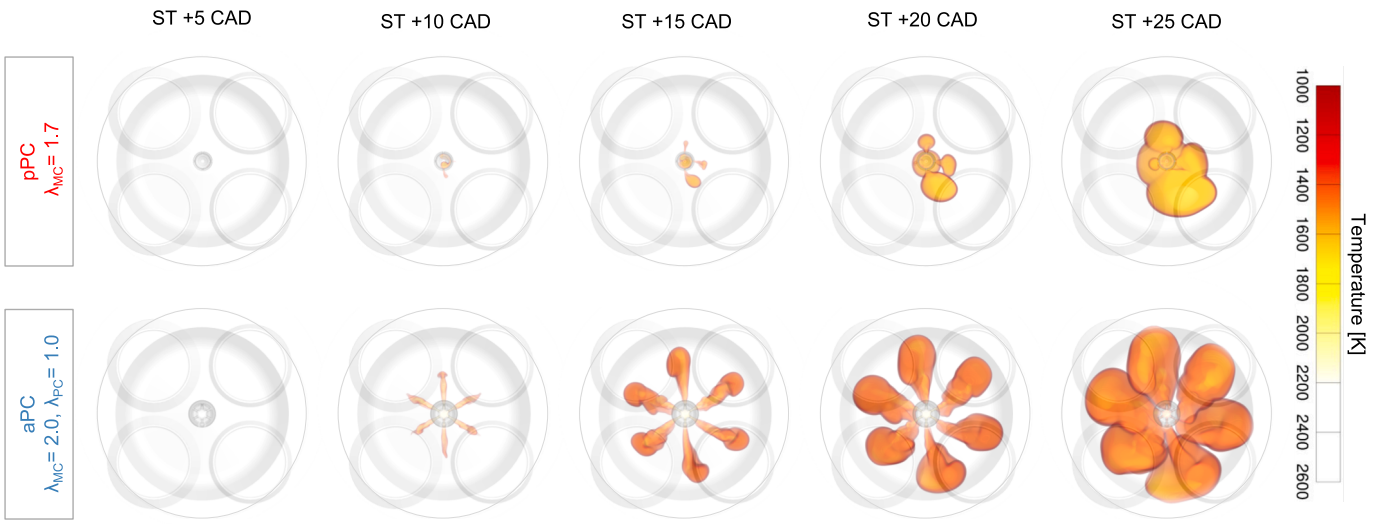

Fig. 7. Temporal evolution of the flame front represented by temperature contours, pPC @ λMC = 1.7, and aPC @ λMC = 2.0, λPC = 1.0.

of the passive and active pre-chamber systems, Fig. 6 shows the pressure and HRR for the two concepts – in red the pPC working with $\lambda_{MC} = 1.7$, while in blue the aPC with $\lambda_{MC} = 2.0$ and $\lambda_{PC} = 1.0$. Dashed lines refer to the pre-chamber, while solid lines refer to the main chamber.

The first main difference lies in the values of the spark timing: $ST_{pPC} = -25$ CAD aTDCf and $ST_{aPC} = -15$ CAD aTDCf. Indeed, the leaner mixture in the pre-chamber for the passive concept results in a lower laminar flame speed for the air–fuel mixture. By examining the HRR in the pre-chamber, a difference of approximately one order of magnitude in the released energy is observed between the two concepts. For this reason, the scale factor of the PC-HRR curves in Fig. 6 (×10) differs from that in Fig. 5 (×100), ensuring consistent visual readability considering the larger energy release in the active case. This higher energy release, driven by the higher volumetric energy density given by the stoichiometric air-to-fuel ratio in the aPC, produces the characteristic pressure peak within the pre-chamber, which is substantially higher than that observed for the pPC. However, it is important to note that the pre-chamber combustion is not fully optimized in either baseline configuration. Indeed, pre-chamber combustion is prolonged, and a significant portion of the heat release occurs after the main-chamber ignition. This behaviour is directly linked to the non-optimized pre-chamber geometries and, in particular, to their relatively large nozzle diameters, which result in high permeability. This effect is especially evident for the active pre-chamber, where the elevated permeability leads to a limited pressure difference between PC and MC ($\Delta p_{PC\text{-}MC}$) of approximately 20 bar, whereas experimental studies on similar aPC systems often report $\Delta p_{PC\text{-}MC}$ values exceeding 40 bar [18]. Further details on this aspect will be discussed in Section 5. Considering MC combustion, the hot jets emerging from the aPC nozzles are more energetic and reactive with respect to pPC, exiting with higher velocity and penetration, and igniting the main-chamber mixture with greater intensity. This behaviour is evident in the HRR of the MC, where the active concept displays a steeper profile, resulting in a markedly shorter combustion duration. It is also worth noting that both main-chamber HRR profiles exhibit a single-stage heat-release behaviour, in contrast to other experimental results available in the literature for engines of comparable bore size, which often display two-stage HRR profiles. Such double-peak profiles are generally attributed to the combined effects of jet–piston interaction and jet-to-jet merging during the MC combustion process. For the pPC concept, the lower pressure difference between the pre-chamber and the main chamber results in less energetic jets, which do not reach the piston or liner surfaces and therefore cannot induce any significant jet–wall interaction. As a result, the flame reaches the chamber walls only during the propagation phase, leading to a single HRR peak. This finding is

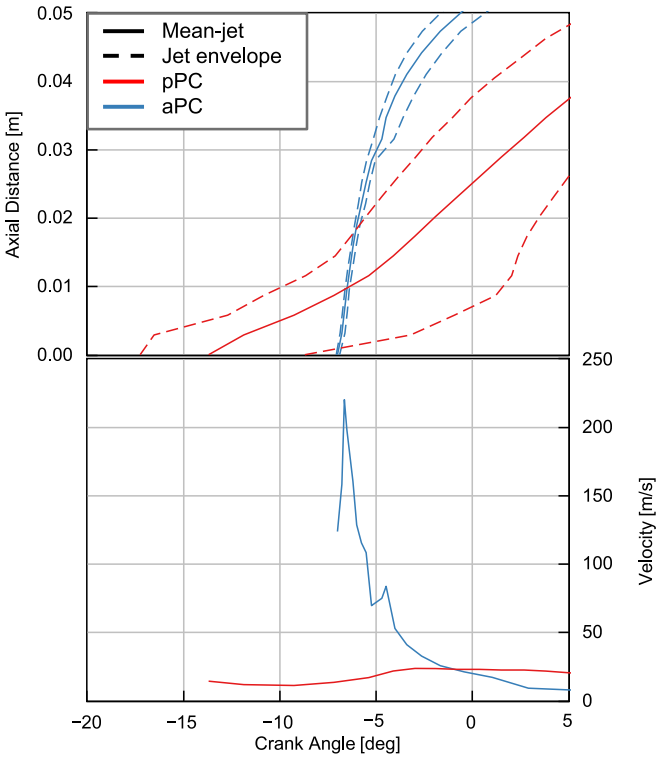

Fig. 8. Jets average penetration (top) and velocity (bottom) for pPC @ λMC = 1.7 in red, and aPC @ λMC = 2.0, λPC = 1.0 in blue. (For interpretation of the references to colour in this figure legend, the reader is referred to the web version of this article.)

consistent with the experimental results obtained on the reference engine equipped with a passive pre-chamber (Accurso et al., [24]), which also exhibited single-stage HRR traces. For the active pre-chamber concept, this phenomenon requires additional clarification, which will be discussed later in this section.

Fig. 7 shows the flame evolution for both concepts (top for passive PC, bottom for active PC) at conditions already shown in Fig. 6. Each figure refers to a specific interval from the spark timing. As previously mentioned, despite the higher volume of the active pre-chamber and the higher distance between spark plug location and PC holes, the jets exit

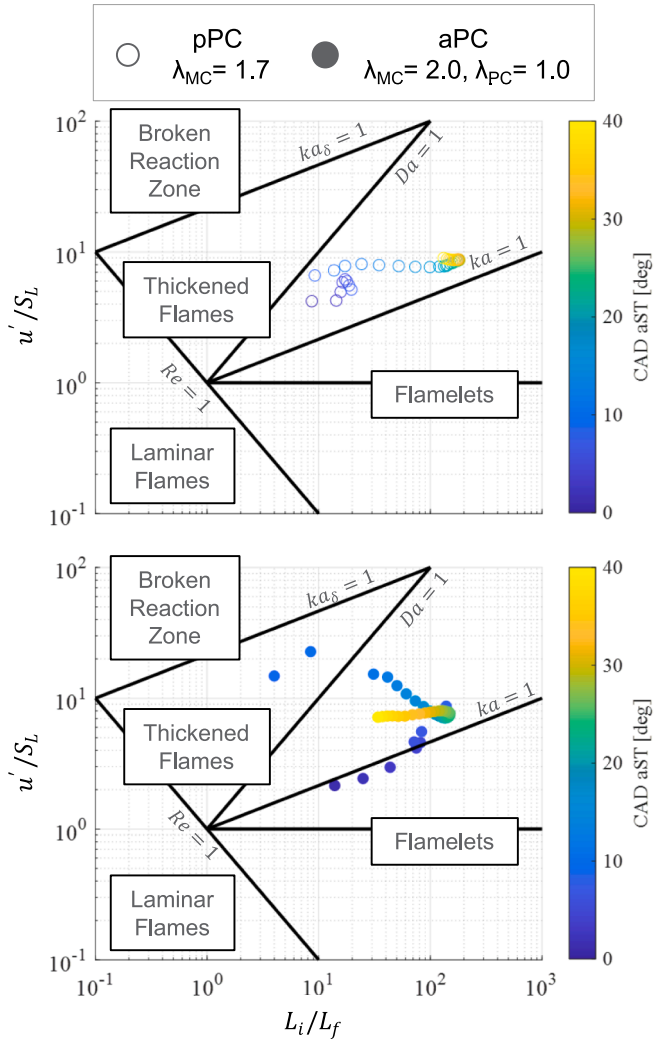

Fig. 9. Turbulent combustion regimes for the pPC @ λMC = 1.7 (top), and aPC @ λMC = 2.0, λPC = 1.0 (bottom).

earlier than the pPC concept due to the significant increase in laminar flame speed that allows rapid and well-distributed flame jet dispersion, covering a wide volume of the combustion chamber. In contrast, jets from passive pre-chamber are slower and less uniform, leading to multi-point ignition in the main chamber predominantly concentrated near the pre-chamber nozzles.

To quantify the different jet dynamics for the two concepts, a detailed analysis of the flame jet propagation has been carried out in Fig. 8. In detail, Fig. 8 – Top shows the axial jet penetration (the solid line is the mean of all the jets, while the dashed lines represent the envelope of the jets), while the lower image shows the average jet velocity. It is evident that jets from active concept penetrate more than the ones exiting from the passive pre-chamber for the abovementioned reasons. In addition, the same reasons allow a reduction in terms of jet-to-jet dispersion, being narrower the area entrained between the two dashed lines. As the jets propagate in the main chamber, jet-to-jet variability increases, since the main chamber flow field influences the jets' uniformity. On the other hand, the pPC is characterized by elevated jet-to-jet variability from the early stage of the ignition process. Jets are characterized by reduced ignition energy and velocity, as a consequence, they are more sensitive to the flow motion in the main chamber and tend to lose the direction given by the nozzles. Hence, the jets penetration is drastically reduced, in comparison with aPC. On a quantitative point of view, in the first stage of jet penetration, when the driver is the flame propagation in the pre-chamber, jets exiting from the passive pre-chamber exhibit a maximum velocity of ~15 m/s, much lower than the one observed in the active concept (~220 m/s). After the ignition of the MC mixture, both concepts show similar velocity in the flame propagation phase because of their similar λ_{MC} values. The velocity levels of the jets shown in Fig. 8 are also consistent with the experimental findings of Guo et al. [56], who investigated hot turbulent jets from an active pre-chamber using double-pass Schlieren imaging. In their study, the authors examined the influence of the orifice diameter, and the measured jet velocities for nozzle sizes comparable to those of the present work were found to be on the order of ~200 m/s, in close agreement with the values predicted by the numerical results of this work. The analysis of jet penetration and velocity is also useful to further support the single-stage HRR profile previously observed for the aPC concept, as reported in Fig. 6. As shown in Fig. 8, the jets impinge on the piston bowl approximately at TDC. By that time, their momentum had already decreased substantially, below the peak values recorded at the nozzle exit. Consequently, the resulting jet–piston interaction occurs with reduced intensity, probably driven by the residual jet inertia. This behaviour is in contrast with the experimental data reported by Liu et al. [57] for a 131 mm bore engine, where the jets reached the piston surface while still carrying near-maximum TKE. Under such conditions, the strong jet–piston interaction contributed to the development of a two-stage HRR. A similar phenomenon was also documented by Rajasegar et al. [58] for a large-bore active pre-chamber system (~140 mm bore), where the HRR exhibited two distinct peaks: the first associated with mixing-controlled combustion driven by the high-momentum jet ejection, and the second, after a stagnation phase, corresponding to a kinetic-controlled combustion phase forming after the merged jets impinged on the piston and separated the main-chamber charge into two burning zones. In the present case study, the longer nozzle-to-piston distance reduces the intensity of the jet–piston interaction, and as shown in Fig. 7, the jets are not yet merged at TDC (ST + 15 CAD). The absence of a unified jet front allows the flame to propagate through the unburned mixture in all directions: radially toward the piston center and chamber walls, and laterally toward the adjacent jets. As a consequence, the conditions required to create multiple distinct burning zones do not develop, and the HRR is characterized by a single-stage profile.

To further understand the different combustion regimes, Fig. 9 shows the development of the flame in the Borghi-Peters diagram for passive (top) and active (bottom) pre-chamber system. It is worth mentioning that Well-Stirred Reactor (WSR) assumption, on which the SAGE combustion model is based, does not intrinsically consider the turbulence chemistry interaction (TCI), therefore the methodology proposed in [30] has been adapted for gaseous fuel and used to define the flame evolution on the Borghi-Peters diagram.

Starting from the ST (highlighted in dark blue), the flame in the active pre-chamber (Fig. 9 – Bottom) evolves in the flamelet region due to high laminar flame speed (S_L) and smaller laminar flame thickness (L_f) which are induced by the near-to-stoichiometric pre-chamber mixture inside the pre-chamber. As the flame propagates toward the pre-chamber nozzles, the mixture entrained by the flame front gets leaner (lower S_L) and therefore the ratio between the turbulent velocity (u') and S_L increases. Simultaneously, the integral length scale (L_i) of the turbulent eddies increases. Hence, the pre-chamber combustion for the aPC system develops toward the thickened flame area of the Borghi diagram, which is characterized by a Karlovitz (Ka) number greater than 1. Then, moving to the main chamber, during the ignition phase the evolution moves close to the broken reaction zone. This is due to the fact that the high speed of the turbulent jets induces an increment of TKE, leading to high u' and small L_i. Then, as the intensity of the turbulent jets produced by the pre-chamber decreases, the combustion is mainly driven by the flame propagation phase. It, indeed, develops towards the thickened flames regions, without reaching the flamelets region due to the dilution of mixture on the flame front. It is evident that lean-operating aPC

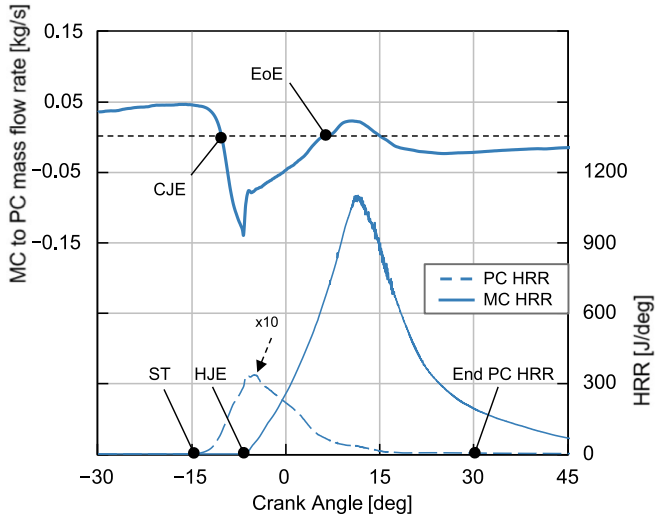

Fig. 10. Temporal evolution of the MC-to-PC mass flow rate (top) and HRR traces for PC and MC (bottom), highlighting the key moments of the pre-chamber energy analysis. Combustion of aPC @ λMC = 2.0, λPC = 1.0, ST = -15 CAD aTDCf.

systems are characterized by a combustion process that spans in different regions of the Borghi diagram.

Moving to the pPC system (Fig. 9 – Top), the combustion develops entirely in the Thickened Flames region. In the initial phase of PC combustion, the low S_L value due to the premixed lean mixture is responsible for a velocity and length scale ratios that lie over the $Ka > 1$ region. During the jet exiting phase, in this case, the reduced intensity of the jets (as shown in Fig. 8) and, thus, the reduced turbulence level limit the evolution towards the broken reaction zone, resulting in a multi-point (torch ignition) ignition pattern, as highlighted by Yang et al. [12]. However, during the flame propagation phase, the two combustion system concepts develop in the same region, the Thickened Flames one, mainly driven by the mixture dilution.

For the purpose of this work, a comparison between the two concepts is carried out in terms of pre-chamber (PC) energy utilization. Taking as reference the methodology proposed by Piano et al. [59] concerning the influence of nozzle geometrical parameters on a gasoline-fueled passive pre-chamber, it is possible to quantify the energy entrained in the PC and to track its release throughout the combustion process. To clarify this energy partitioning, Fig. 10 illustrates the most representative phases of a typical pre-chamber combustion event, summarized as follows:

- Spark Timing (ST): corresponding to the ignition event, identifiable by the initial rise of the PC HRR.
- Cold Jet Ejection (CJE): the onset of flow reversal from MC to PC due to the pressure increase inside the PC, resulting in the ejection of unburned mixture.
- Hot Jet Ejection (HJE): the moment when reactive jets ignite the MC mixture, identifiable by the rise of the HRR in the MC.
- End of Ejection (EoE): the point at which flow reversal occurs again in the PC nozzles, as the MC pressure exceeds that of the PC.
- End PC HRR is reached when the heat release rate curve approaches zero, indicating that combustion within the pre-chamber is complete.

Following the definition of these key timings, the corresponding energy contributions can be established. Fig. 11 (left) reports the energy entrained in the PC, subdivided into three main components:

- Fuel Power at ST (FP at ST): fuel energy contained in the PC at the spark event.

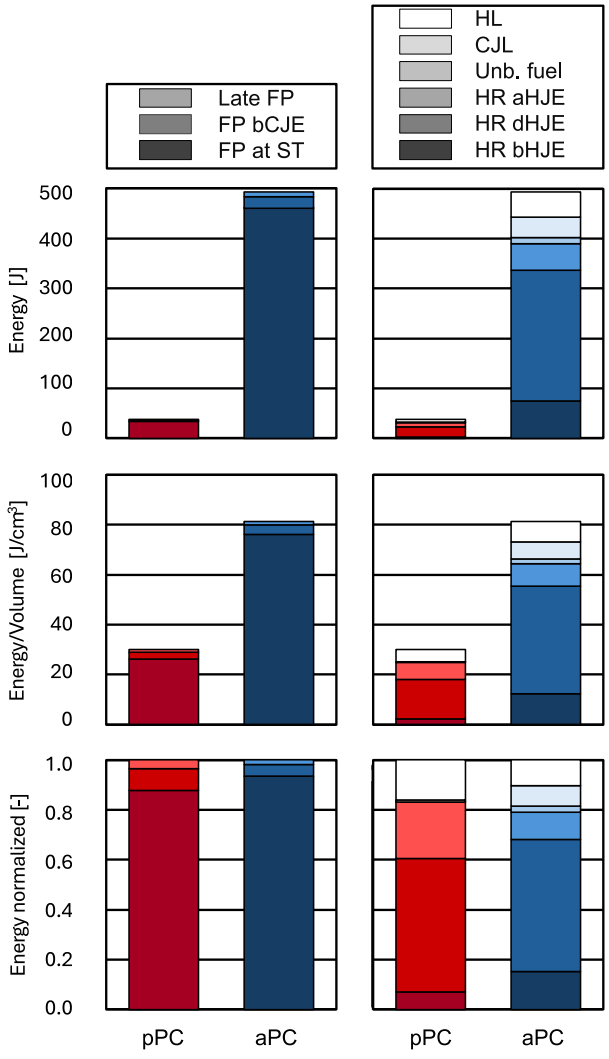

Fig. 11. Pre-chamber energy analysis for pPC @ λMC = 1.7 in red bars, and aPC @ λMC = 2.0, λPC = 1.0 in blue bars. Absolute energy content (Top), Energy per unit of volume (Middle), Normalized energy (Bottom). (For interpretation of the references to colour in this figure legend, the reader is referred to the web version of this article.)

- Fuel Power before CJE (FP bCJE): fuel energy entering the PC between ST and CJE.
- Late Fuel Power (Late FP): fuel energy entering the PC after EoE.

On the right side of Fig. 11, the PC combustion energy utilization is divided into six contributions:

- Heat Release before HJE (HR bHJE): cumulative energy released in the PC from ST to HJE.
- Heat Release during HJE (HR dHJE): cumulative energy released between HJE and EoE.
- Heat Release after HJE (HR aHJE): cumulative energy released after the HJE phase.
- Cold Jet Losses (CJL): fuel energy expelled during the CJE phase, up to HJE.
- Heat Losses (HL): energy dissipated through heat transfer to the PC walls, from ST to End PC HRR.
- Unburned Fuel Energy: residual fuel energy remaining in the PC after combustion.

It is worth noting that only HR bHJE and HR dHJE contribute

directly to the energy of the jets responsible for main chamber ignition. Although cold jets reduce the pre-chamber fuel energy, this energy is subsequently released during MC combustion and also contributes to the enhancement of turbulence prior to hot jet ignition. All other terms are considered as energy losses.

In this work, the comparison between the active (aPC) and passive (pPC) configurations is presented from top to bottom in Fig. 11, in terms of absolute energy, energy density, and normalized energy. At the top, the markedly higher energy content of the aPC is evident. This outcome results from both its larger volume (VaPC ≈ 4 × VpPC) and its stoichiometric mixture, while the pPC operates approximately at $\lambda_{PC} = 1.7$, corresponding to λ_{MC} value. Consequently, the total fuel energy available in the aPC exceeds that of the pPC by more than an order of magnitude. In the middle section, the aPC shows a higher energy density, mainly attributed to its richer mixture. The energy associated with FP bCJE, representing the fuel entering the PC from ST to CJE, is higher in both absolute and specific terms for the aPC. This result is somewhat counterintuitive considering that the MC mixture is more diluted ($\lambda_{MC} = 1.7$ for pPC, $\lambda_{MC} = 2.0$ for aPC). However, without specific optimization of the aPC injection system—particularly spray targeting and timing—fuel escape from the PC can occur. In such conditions, fresh fuel pockets are often observed near the orifices and may re-enter the PC during the final compression phase (i.e. between ST and CJE). For the same PC volume, the aPC configuration thus stores a greater amount of energy beneficial to MC ignition, as highlighted by the pronounced increase in HR bHJE, which governs the pressure differential between PC and MC. While this pressure rise enhances the penetration and intensity of the hot jets, it simultaneously increases CJL, which become significant in the aPC case. Hence, accurate optimization of injector targeting is essential. Numerical results indicate that concentrating the injected mass into a near-stoichiometric cloud around the spark region can simultaneously reduce Cold Jets losses and dilute the overall pre-chamber mixture, potentially improving NOx emissions. At the bottom of Fig. 11, the comparison is reported in terms of normalized energy fractions. The aPC exhibits a larger portion of energy associated with the fuel already present at ST and a reduced fraction entering after ST and EoE, indicating that a greater share of the fuel energy is available from the very beginning of the PC combustion process. The combined contribution of HR bHJE and HR dHJE, representing the effective energy driving MC ignition, is higher for the aPC, confirming its superior energy conversion efficiency. The richer mixture in the aPC promotes faster flame propagation and a shorter combustion duration, which consequently reduces the fraction of HR aHJE compared with the pPC case. Similarly, the heat loss fraction is higher for the pPC, despite its smaller surface area and lower PC temperatures. This behaviour is primarily attributed to the longer combustion duration of the pPC, which increases the exposure time for heat transfer. Conversely, the pPC proves advantageous in terms of CJL and unburned fuel energy, both of which are lower than in the aPC. The higher unburned fuel fraction observed in the aPC originates from its more complex geometry—accommodating both the injector and the spark plug—which can generate regions that are less accessible to the propagating flame front.

5. Results: combustion optimization

After the comprehensive analysis of the combustion process of the two systems and a preliminary overview of their potentialities and limitations, the optimization of the two systems was performed. The optimization focused mainly on the design of the pre-chambers. Several pre-chamber designs were tested for both concepts. Among them, in the present work, results concerning only two of them (one for the pPC and one for the aPC) are reported for the sake of brevity, and the main modifications are listed in Table 2. In addition, a dedicated optimization of the calibration was carried out to achieve the maximum potential of each system.

Starting from pPC concept, the optimized geometry features a higher number of holes, having an orientation to induce swirl within the main chamber. The holes diameter has been reduced to keep the A_{nozzle}/V_{PC} ratio almost constant. Fig. 12 illustrates the impact of the different design on the pressure and HRR for both main chamber (solid lines) and pre-chamber (dashed lines). Red lines refer to the baseline PC geometry, while the orange lines refer to the optimized version. In the main chamber, the optimized geometry leads to a higher and advanced HRR peak, indicating accelerated combustion and improved ignition effectiveness. This enhanced performance is attributed to the revised nozzle layout, specifically the introduction of six swirling tilted holes, which promote turbulence generation in the main chamber.

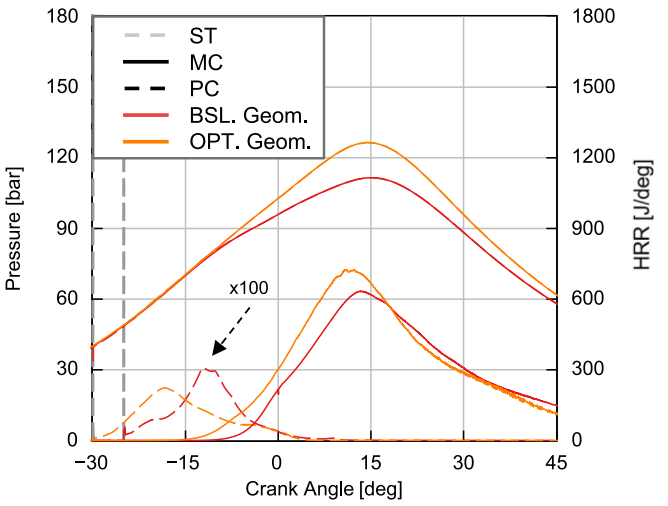

Fig. 12. Pressure and HRR profiles of baseline (red) and optimized (orange) passive pre-chamber geometries @ λMC = 1.8. (For interpretation of the references to colour in this figure legend, the reader is referred to the web version of this article.)

Interestingly, despite the lower energy released in the pre-chamber (as highlighted by the reduced dashed orange curve), the system as a whole performs better. This is because the reduction in pre-chamber volume, along with the appropriately scaled nozzle area, ensures a favourable balance between ignition energy distribution and jet velocity, optimizing flame propagation dynamics.

The critical insight lies in the possibility of advancing spark timing, and efficiently obtaining an MFB50 advance even with reduced fuel energy inside the pPC. Due to the more advanced spark timing (ST = –30 CAD) employed in the optimized case, the fuel mass trapped in the pre-chamber at ignition is reduced, since less time is available for PC scavenging during the late compression stroke. As a result, the overall energy released in the pre-chamber is lower. Nevertheless, the first phase of ignition in MC is characterized by similar gradients of HRR curves, meaning that the useful ignition energy is similar for the two geometries. Thus, the optimized version is able to convert a higher fraction of the entrained fuel energy into useful ignition energy.

In the active concept, the optimized geometry features a reduced PC volume together with a significant decrease in hole diameter, which results in a net reduction of the A_{nozzle}/V_{PC} ratio. The numerical analysis has been carried out considering $\lambda_{MC} = 2.0$ and $\lambda_{PC} = 1.0$. The reduction of the PC volume implies a reduction of the chemical energy trapped in the PC, while the decrease in hole diameter leads to a marked reduction in pre-chamber permeability. As shown experimentally in the work of Shah et al. [60], lower A_{nozzle}/V_{PC} ratios promote a stronger confinement of the PC mixture and generate higher $\Delta p_{PC\text{-}MC}$. In [60] it was also highlighted that the A_{nozzle}/V_{PC} ratio plays a more dominant role in determining the pressure rise than the ratio V_{PC}/V_{TDC}. For A_{nozzle}/V_{PC} ratios comparable to those of the pre-chamber optimized configuration shown in the present work, Shah et al. reported maximum pressure differences of approximately 20–25 bar. However, these measurements

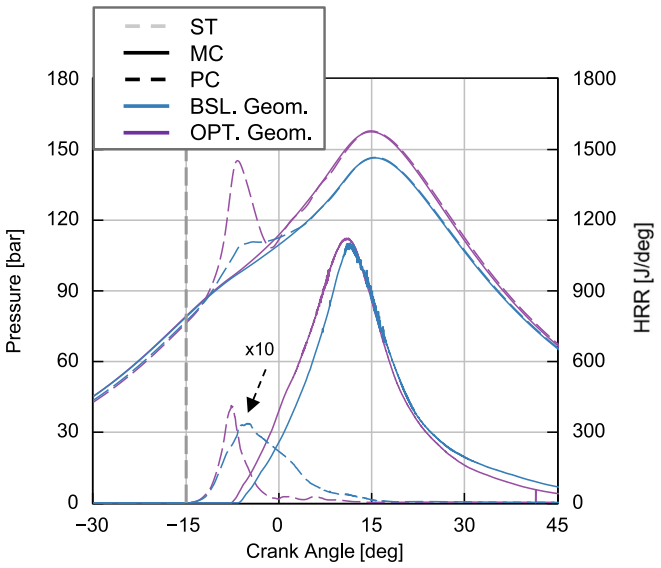

Fig. 13. Pressure and HRR profiles of baseline (blue) and optimized (purple) active pre-chamber geometries @ λMC = 2.0, λPC = 1.0. (For interpretation of the references to colour in this figure legend, the reader is referred to the web version of this article.)

were obtained at medium-load conditions (IMEP ≈ 10–12 bar). Under high-load conditions, higher PC fuel energy for fixed mixture dilution is expected to produce substantially larger pressure rises. In the present study, the reduction of A_{nozzle}/V_{PC} is further amplified by the substantial reduction of the nozzle diameter, which significantly limits the interaction between the two chambers. The results are clearly visible in Fig. 13, where the optimized geometry shows a marked increase in Δp_{PC-MC}, up to ~50 bar. For high-load operations, in the experimental work of Eicheldinger et al. [18], an active pre-chamber with a V_{PC}/V_{TDC} ratio of 2.4 % has been employed, featuring an aPC volume comparable with that of the optimized design analysed in the present work. Their analysis demonstrates that pre-chambers of such size can generate pressure differences on the order of 50 bar, in agreement with the numerical results presented in this study. To conclude, despite the lower fuel energy stored in the optimized configuration, the increased confinement enables a more efficient combustion inside the pre-chamber, which burns the entire in-pre-chamber charge with a sharp and narrow HRR profile. In the main chamber, this leads to an advanced start of combustion, even if the spark timing has been kept constant. This eventually results in a more efficient and faster combustion process.

The combustion behaviour observed in Fig. 13 is further supported by the temperature field evolution shown in Fig. 14, which captures the development of pre-chamber jets at successive crank angles (from ST + 10 CAD to ST + 30 CAD) for both baseline (top row) and optimized (bottom row) PC geometries.

At ST + 10 CAD, optimized configuration shows a slight advance in hot jets exiting from the pre-chamber, with higher penetration. By ST + 15 and + 20 CAD, the optimized case clearly exhibits larger and more advanced high-temperature zones, suggesting stronger jet penetration and better flame propagation. These jets enable a broader and more uniform ignition front. By ST + 25 CAD, the flame front in the optimized configuration has already reached a more developed shape which envelops a larger mixture volume, while the flame achieved with the baseline PC flame is slightly more confined and less uniformly distributed. This is in accordance with the reduced combustion duration previously mentioned.

The comparison in Fig. 15 summarizes the results achieved in terms of combustion indicators and specific emissions with the geometry optimization process. For the passive configuration, the optimized geometry results in a more advanced MFB50, consistent with the earlier and faster HRR commented previously. This aspect, combined with the reduction of the combustion duration, expressed as MFB10-75, contributes to the achievement of the target load, and a drastic increment of ITE up to ~ 44 %. At the same time, the optimized pPC geometry leads to a notable decrease in uHC thanks to the faster flame propagation and reduced quenching. On the other hand, NOx emissions increase, likely due to higher local temperatures and pressure, caused by an advanced combustion phasing and increased load. Nevertheless, a fairer comparison should be made between the baseline and optimized pPC at a fixed load. Hence, referring back to Fig. 4, considering baseline pPC working at $\lambda_{MC} = 1.7$, it is possible to reduce total NOx emissions by ~ 50 % with optimized geometry with swirling nozzles. This drastic reduction is mainly due to the extension of the lean limit, which allows the optimized geometry to reach the target load working with a higher $\lambda_{MC} = 1.8$. Concerning the active pre-chamber concept, the geometry optimization process leads to a reduction of both MFB50 and MFB1075, together with a non-negligible increase in IMEP and a significant improvement in ITE, reaching a peak value of 46.9 %. Moreover, the most significant improvements achieved with the optimized geometry are related to specific emissions, particularly ISNOx and ISHC. The shorter combustion

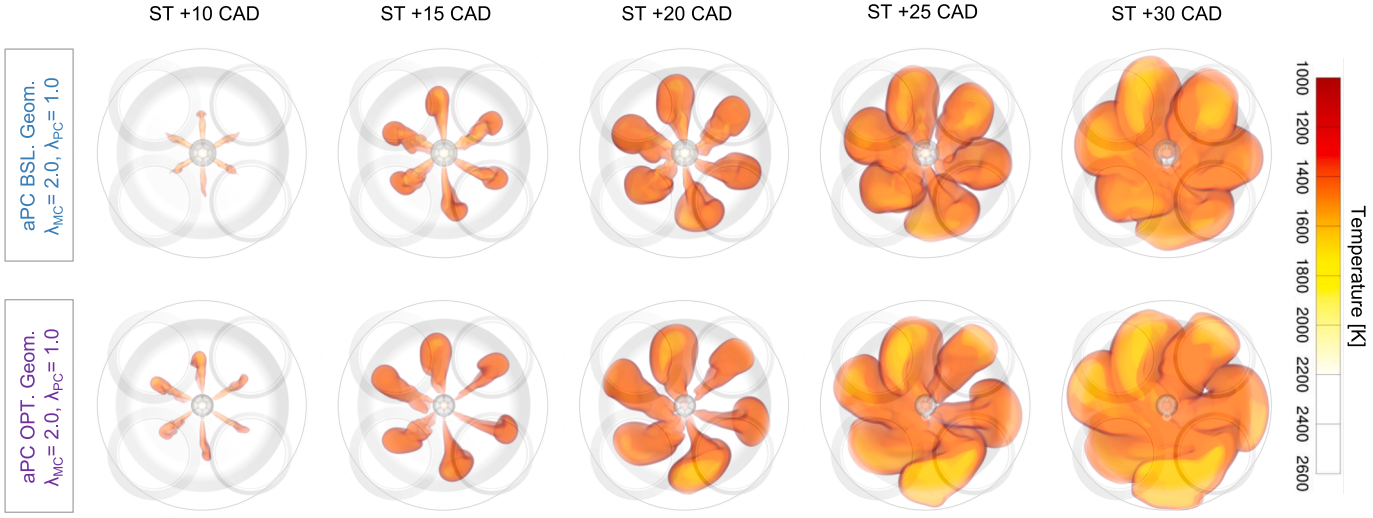

Fig. 14. Temporal evolution of the flame front represented by temperature contours for the baseline (top) and optimized (bottom) active pre-chamber geometries @ λMC = 2.0, λPC = 1.0.

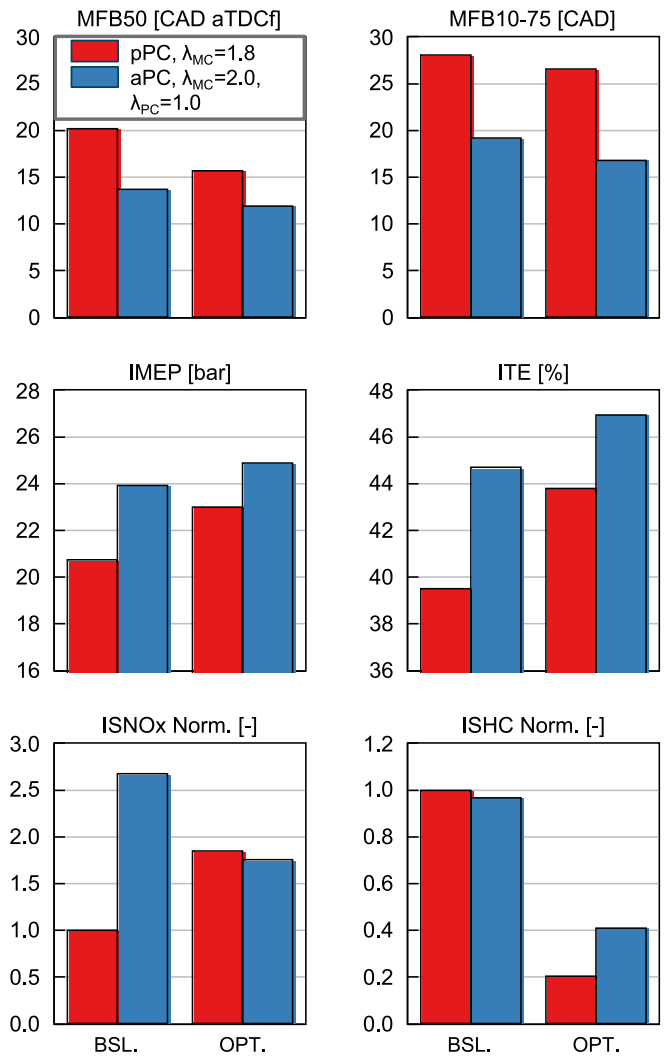

Fig. 15. Results in terms of combustion, performance and emissions of the geometry optimization process. Red bars refer to passive pre-chamber concept @ λMC = 1.8; blue bars refer to active pre-chamber concept @ λMC = 2.0, λPC = 1.0. Emissions have been normalized with respect to results obtained with pPC concept at λMC = 1.8, baseline geometry. (For interpretation of the references to colour in this figure legend, the reader is referred to the web version of this article.)

duration strongly reduces the formation of unburnt hydrocarbons, which are approximately halved with respect to the baseline geometry. With regard to NOx emissions, the optimized aPC shows a clear improvement despite the higher peak pressures and temperatures both in MC and PC, which would normally promote NOx formation. The key driver of this result is the reduced volume of the optimized pre-chamber, which significantly limits the amount of NOx formed inside the PC itself. As shown previously in Fig. 4, at $\lambda_{MC} = 2.0$ and $\lambda_{PC} = 1.0$, the baseline aPC accounted for approximately 55 % of the total engine-out NOx. By reducing the pre-chamber volume, NOx produced inside the PC decreases by roughly 40 %, and this reduction more than compensates for the moderate increase in NOx generated in the main chamber. As a result, the overall engine-out NOx emissions decrease by ~ 34 % compared with the baseline aPC geometry.

The increased complexity of the active concept is due to both hardware characterization and the increased number of engine calibration parameters. Indeed, thanks to the direct fuelling of the pre-chamber, it is possible to change SOI, energizing time, and even fuel mass quantity. For this reason, it is not even necessary to work with a globally stoichiometric pre-chamber mixture in all the operating conditions. For

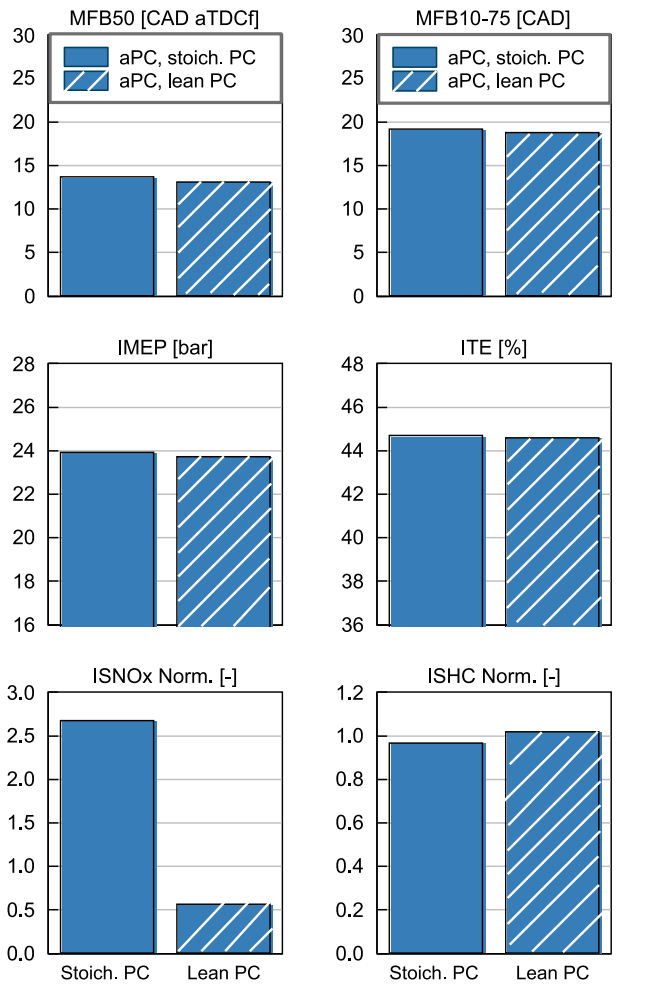

Fig. 16. Comparison of combustion, performance and emissions for stoichiometric and lean aPC concept. Emissions have been normalized with respect to results obtained with pPC concept at λMC = 1.8, baseline geometry to keep consistency with previously mentioned results.

demonstration purposes only, some investigations have been carried out reducing the amount of fuel injected in the pre-chamber, thus leading to an overall leaner PC mixture. Working with the same reference operating conditions ($\lambda_{MC} = 2.0$), the λ_{PC} value has been increased from 1.0 to 1.5. At this stage, tuning of spark timing was necessary, with the leaner pre-chamber that required some CADs of ST advance. Results of the two concepts are reported in Fig. 16. It is noticeable that it was possible to achieve the same results in terms of combustion indicators with the tuning of the spark timing, and simultaneously to drastically decrease the total NOx emissions. The reasons behind such a reduction are similar to what has been described in the previous section. When the pre-chamber itself is responsible for more than 50 % of total NOx emissions, it is clear that optimization should be addressed to this part of the system. The optimization process can be targeted to geometry characteristics or tuning of calibration parameters (or both), with the same goal of reducing the NOx that are formed inside the PC. In this case, a leaner λ value in the PC is responsible for a reduction of total NOx emissions of ~ 70 %. On the other hand, the increase of λ inside the pre-chamber is responsible for a slight increase in unburnt hydrocarbons. These results are aligned with [21] which experimentally assessed the impact of λ_{PC} values on combustion indicators and emissions. In [21], evaluations related to CoV showed that increasing λ_{PC} value is connected to an increment of CoV_{IMEP} that ultimately poses a significant limit on the PC enleanment process. It is worth mentioning that in this work, cycle-by-cycle has not been considered as a limiting factor since RANS

simulation approach does not allow any analysis of cyclic variability.

6. Conclusions

This work presented a comprehensive numerical investigation of passive (pPC) and active (aPC) pre-chamber combustion systems for high-speed, large-bore methane engines, with the objective of exploring their limitations and potential in lean-burn operation.

The ultimate goal of this research is to support the development of a Large Bore engine platform for marine propulsion and generator set applications, capable of achieving IMO Tier III NO_x emission limits without relying on exhaust after-treatment systems. The study was divided into two main phases: first, a comparative analysis was performed to understand fundamental differences between the two innovative ignition concepts; second, a dedicated optimization campaign was carried out to explore performance enhancement opportunities via geometric and calibration parameters tuning.

In the first part of the study, the passive pre-chamber system, while mechanically simpler and more suited to retrofitting existing diesel engine architectures, showed significant drawbacks when operating at high λ_{MC} values. These limitations are primarily linked to the inability to control combustion phasing through spark timing alone, due to the fully lean composition of the PC mixture. As spark timing is advanced, the amount of fuel energy in the pre-chamber decreases significantly, leading to a drop in ignition energy, weakening the intensity of hot turbulent jets and resulting in longer combustion durations (MFB10–75) and delayed MFB50. In contrast, the active pre-chamber concept shows superior robustness under lean conditions. Direct injection allows the formation of richer pre-chamber mixtures, enabling faster and more penetrating jets that effectively centre MFB50 values even at $\lambda_{MC} > 2.0$. This capability translated into higher indicated thermal efficiencies (ITE) and extended lean operability beyond what was achievable with the passive system.

To understand the origin of this performance gap, three complementary analyses were conducted:

Energetic analysis revealed that the aPC stored significantly more fuel energy. Moreover, a greater fraction is effectively converted into useful heat release before and during hot jet ejection.
Jet dynamics showed higher jet velocities and more homogeneous penetration patterns in aPC systems, supporting faster main chamber ignition and reduced sensitivity to main chamber turbulence.
Combustion regime classification using Borghi plots indicated that, under high λ_{MC} operation, aPC systems operate in regimes characteristic of Turbulent Jet Ignition (TJI) – Damköhler ~ 1. In contrast, the hot jet ignition phase of pPC systems is characterized by lower turbulence intensity, resulting in a multi-point (torch ignition) ignition pattern. These results are in agreement with [12].

Following this comparative assessment, a geometry optimization campaign was performed for both systems using 3D-CFD:

- For the passive pre-chamber, a swirling nozzle configuration enabled effective phasing at $\lambda_{MC} = 1.8$, allowing ITE to reach ~44 % while achieving a 50 % NO_x reduction compared to the baseline pPC operating with $\lambda_{MC} = 1.7$, due to the extension of the lean limit.
- For the active pre-chamber, the volume and nozzle diameter reduction allows for advancing the combustion phasing without triggering knock and yielded a peak ITE of 46.9 %, along with a ~34 % NO_x decrease relative to the baseline aPC.

It is also worth noting that, unlike the passive concept, the active pre-chamber allows direct control of the local air-to-fuel ratio (λ_{PC}). As a demonstrative case, increasing λ_{PC} from stoichiometric to 1.5 led to a 70 % reduction in total NO_x emissions, without compromising combustion performance.

In conclusion, this work demonstrates that both passive and active pre-chamber systems can be effectively tailored through geometry and calibration to meet the dual challenge of high efficiency and low NO_x emissions in lean methane engines. Innovative combustion systems as passive and active pre-chambers show great potential when coupled with 3D-CFD-driven design, making them strong candidates for future ultra-low emission engine architectures.

CRediT authorship contribution statement

Federico Millo: Writing – review & editing, Funding acquisition. **Massimiliano Zanatta:** Writing – original draft, Visualization, Methodology, Investigation, Formal analysis, Data curation, Conceptualization. **Andrea Scalambro:** Writing – review & editing, Methodology, Investigation, Conceptualization. **Andrea Piano:** Writing – review & editing, Supervision, Project administration, Methodology, Investigation, Conceptualization. **Francesco Accurso:** Writing – review & editing, Supervision, Project administration, Investigation, Conceptualization. **Francesco C. Pesce:** Conceptualization, Writing - Review & Editing, Supervision, Funding acquisition. **Alberto L. Vassallo:** Writing - Review & Editing, Supervision, Project Administration, Funding acquisition.

Declaration of competing interest

The authors declare that they have no known competing financial interests or personal relationships that could have appeared to influence the work reported in this paper.

Acknowledgements

The research presented in this paper was performed within the project: "*Propulsione a combustibili alternativi per raggiungere la massima decarbonizzazione nel settore marino*" funded by "*Ministero delle Imprese e del Made in Italy*" inside call "*Accordi per l'innovazione*" and approved by "*Decreto n. 326 del 29/04/2024*"

Data availability

The data that has been used is confidential.

References

[1] International Energy Agency, Net Zero by 2050 - A Roadmap for the Global Energy Sector, 2021.
[2] IMO - MARPOL Annex VI, https://www.imo.org/en/ourwork/environment/pages/index-of-mepc-resolutions-and-guidelines-related-to-marpol-annex-vi.aspx.
[3] International Maritime Organization, Regulation 13: Nitrogen Oxides Emission Limits under MARPOL Annex VI, https://www.imo.org/en/ourwork/environment/pages/nitrogen-oxides-(nox)-%E2%80%93-regulation-13.aspx.
[4] Bouman EA, Lindstad E, Rialland AI, Strømman AH. State-of-the-art technologies, measures, and potential for reducing GHG emissions from shipping – a review. Transp Res D Transp Environ May 2017;52:408–21. https://doi.org/10.1016/j.trd.2017.03.022.
[5] DNV - Maritime Forecast to 2050, https://www.dnv.com/maritime/maritime-forecast/.
[6] I. E. A. (IEA), World Energy Outlook 2020. 2020. [Online]. Available: https://www.iea.org/reports/world-energy-outlook-2020.
[7] Ju D, Huang Z, Li X, Zhang T, Cai W. Comparison of open chamber and pre-chamber ignition of methane/air mixtures in a large bore constant volume chamber: effect of excess air ratio and pre-mixed pressure. Appl Energy Feb. 2020; 260. https://doi.org/10.1016/j.apenergy.2019.114319.
[8] A. Kirkpatrick, G.-H. Kim, D. Olsen, CFD modeling of the performance of a prechamber for use in a large bore natural gas engine, in ASME - ICES2005, 2005. doi: 10.1115.
[9] Toulson E, Schock H, Attard W. A review of pre-chamber initiated jet ignition combustion systems. SAE Technical Paper 2010-01-2263 2010.
[10] Thelen BC, Toulson E. A computational study of the effects of spark location on the performance of a turbulent jet ignition system. In: SAE Technical Papers. SAE International; 2016. https://doi.org/10.4271/2016-01-0608.
[11] Warnatz J, Maas U, Dibble RW. Combustion. 3rd ed. Berlin-Heidelberg-New York: Springer; 1997.

[12] Yang X, Li G, Wang P, Cheng Y, Zhao Y. Numerical investigation of the operating characteristics of the passive and active prechamber jet ignition in a natural gas engine. ACS Omega Jul. 2024;9(29):31933–45. https://doi.org/10.1021/acsomega.4c03587.
[13] A. Shah, Improving the Efficiency of Gas Engines using Pre-chamber Ignition, Lund University, 2015. [Online]. Available: https://portal.research.lu.se/en/publications/improving-the-efficiency-of-gas-engines-using-pre-chamber-ignitio.
[14] Gentz G, et al. A study of the influence of orifice diameter on a turbulent jet ignition system through combustion visualization and performance characterization in a rapid compression machine. Appl Therm Eng Jul. 2015;81. https://doi.org/10.1016/j.applthermaleng.2015.02.026.
[15] Li F, Zhao Z, Wang Z, Wang B. Experimental and numerical study of a methane-fueled pre-chamber system in rapid compression machine. Combust Sci Technol 2021;193(9):1463–94. https://doi.org/10.1080/00102202.2019.1699547.
[16] Shapiro E, et al. Experimental and numerical analysis of pre-chamber combustion systems for lean burn gas engines. In: SAE Technical Papers. SAE International; 2019. https://doi.org/10.4271/2019-01-0260.
[17] Lu C, Song E, Xu C, Ni Z, Yang X, Dong Q. Analysis of performance of passive pre-chamber on a lean-burn natural gas engine under low load. J Mar Sci Eng 2023;11:3. https://doi.org/10.3390/jmse11030596.
[18] Eicheldinger S, et al. BMEP > 30 bar with Gas Engines. 27th Aachen Colloquium Automobile and Engine Technology 2018. 2018.
[19] Technical Instructions on Air Quality Control – TA Luft. [Online]. Available: https://www.bmuv.de/fileadmin/Daten_BMU/Download_PDF/Luft/taluft_engl.pdf.
[20] Dieselnet.com: Germany Stationary Engines, https://dieselnet.com/standards/de/taluft.php.
[21] Shah A, Tunestal P, Johansson B. Effect of relative mixture strength on performance of divided chamber 'Avalanche activated combustion' Ignition technique in a heavy duty natural gas engine. In: SAE Technical Papers. SAE International; 2014. https://doi.org/10.4271/2014-01-1327.
[22] Shah A, Tunestal P, Johansson B. Investigation of performance and emission characteristics of a heavy duty natural gas engine operated with pre-chamber spark plug and dilution with excess air and EGR. SAE Int J Engines 2012;5(4):1790–801. https://doi.org/10.4271/2012-01-1980.
[23] Accurso F, Pesce FC, Gorietti V, Buzzi L, Marchitto L, Giardino A. Development of a flexible high-speed single cylinder engine platform for natural gas and methanol combustion optimization. WTZ - 13th Conference Injection and Fuels. 2025.
[24] Marchitto L, Pesce F, Accurso F, Tornatore C. Experimental and numerical study on the performance and exhaust emissions of a single-cylinder natural gas large bore engine equipped with passive pre-chamber. SAE Technical Paper 2025-24-0022 2025.
[25] S. J. Jeong, S. Seo, and S. J. Moon, CFD simulation of pre-chamber spark-ignition large bore CNG engine: model development, practical applications, and experimental validation, Energies (Basel), 18, 7, 2025, doi: 0.3390/en18071600.
[26] Novella R, Gomez-Soriano J, Barbery I, Libert C. Numerical analysis of the passive pre-chamber ignition concept for light duty applications. Appl Therm Eng 2022;213:118610. https://doi.org/10.1016/j.applthermaleng.2022.118610.
[27] Ge H, Bakir AH, Yadav S, Kang Y, Parameswaran S, Zhao P. CFD optimization of the pre-chamber geometry for a gasoline spark ignition engine. Front Mech Eng Jan. 2021;6. https://doi.org/10.3389/fmech.2020.599752.
[28] Xu G, Hanauer C, Wright YM, Boulouchos K. CFD-simulation of ignition and combustion in lean burn gas engines. In: SAE Technical Papers. SAE International; 2016. https://doi.org/10.4271/2016-01-0800.
[29] Kim J, Scarcelli R, Som S, Shah A, Biruduganti MS, Longman DE. Numerical investigation of a fueled pre-chamber spark-ignition natural gas engine. Int J Engine Res Sep. 2022;23(9):1475–94. https://doi.org/10.1177/14680874211020180.
[30] Piano A, et al. CFD-based methodology for the characterization of the combustion process of a passive pre-chamber gasoline engine. Transp Eng Sep. 2023;13. https://doi.org/10.1016/j.treng.2023.100200.
[31] Di Sabatino F, Martinez-Hernandiz PJ, Rosa RN, Ekoto I. Investigation of the effects of passive pre-chamber nozzle pattern and ignition system on engine performance and emissions. Int J Engine Res 2022;24(6):2592–613. https://doi.org/10.1177/14680874221129331.
[32] Martinez-Hernandiz PJ, Di Sabatino F, Novella R, Ekoto I. A Numerical and experimental investigation on different strategies to evaluate heat release rate and performance of a passive pre-chamber ignition system. In: SAE Technical Papers. SAE International; 2022. https://doi.org/10.4271/2022-01-0386.
[33] Shah A, Tunestal P, Johansson B. Scalability aspects of pre-chamber ignition in heavy duty natural gas engines. In: SAE Technical Papers. SAE International; 2016. https://doi.org/10.4271/2016-01-0796.
[34] Yamanaka K, Shiraga Y, Nakai S. Development of pre-chamber sparkplug for gas engine. SAE Technical Paper 2011-01-1870 2011. https://doi.org/10.4271/2011-01-1870.
[35] CONVERGE CFD Software, https://convergecfd.com/.
[36] University of California at San Diego, San Diego Mechanism, https://web.eng.ucsd.edu/mae/groups/combustion/mechanism.html.
[37] Han Z, Reitz RD. Turbulence modeling of internal combustion engines using RNG κ-ε models. Combus Sci Technol 1995;106(4–6):267–95. https://doi.org/10.1080/00102209508907782.
[38] A. A. Amsden, P. J. O'Rourke, and T. D. Butler, KIVA-II: A computer program for chemically reactive flows with sprays, May 1989. doi: https://doi.org/10.2172/6228444.
[39] Silva M, et al. Computational assessment of effects of throat diameter on combustion and turbulence characteristics in a pre-chamber engine. Appl Therm Eng Jul. 2022;212:118595. https://doi.org/10.1016/J.APPLTHERMALENG.2022.118595.
[40] Wärtsilä Methane Number Calculator, https://www.wartsila.com/marine/products/gas-solutions/methane-number-calculator.
[41] GT-Suite webpage, https://www.gtisoft.com/gt-suite/.
[42] Zhang P, Zsély IG, Samu V, Nagy T, Turányi T. Comparison of methane combustion mechanisms using shock tube and rapid compression machine ignition delay time measurements. Energy Fuels Aug. 2021;35(15):12329–51. https://doi.org/10.1021/acs.energyfuels.0c04277.
[43] Zhang P, Zsély IG, Papp M, Nagy T, Turányi T. Comparison of methane combustion mechanisms using laminar burning velocity measurements. Combust Flame Apr. 2022;238. https://doi.org/10.1016/j.combustflame.2021.111867.
[44] University of Galway, AramcoMech 2.0, https://www.universityofgalway.ie/combustionchemistrycentre/mechanismdownloads/aramcomech20/.
[45] Metcalfe WK, Burke SM, Ahmed SS, Curran HJ. A hierarchical and comparative kinetic modeling study of C1–C2 hydrocarbon and oxygenated fuels. Int J Chem Kinet 2013;45(10):638–75. https://doi.org/10.1002/kin.20802.
[46] Kéromnès A, et al. An experimental and detailed chemical kinetic modeling study of hydrogen and syngas mixture oxidation at elevated pressures. Combust Flame Jun. 2013;160(6):995–1011. https://doi.org/10.1016/J.COMBUSTFLAME.2013.01.001.
[47] Li Y, Zhou CW, Somers KP, Zhang K, Curran HJ. The oxidation of 2-butene: a high pressure ignition delay, kinetic modeling study and reactivity comparison with isobutene and 1-butene. Proc Combust Inst Jan. 2017;36(1):403–11. https://doi.org/10.1016/J.PROCI.2016.05.052.
[48] Konnov AA. Implementation of the NCN pathway of prompt-NO formation in the detailed reaction mechanism. Combust Flame Nov. 2009;156(11):2093–105. https://doi.org/10.1016/J.COMBUSTFLAME.2009.03.016.
[49] Li X, et al. Pre-chamber turbulent jet ignition of methane/air mixtures with multiple orifices in a large bore constant volume chamber: effect of air-fuel equivalence ratio and pre-mixed pressure. Front Energy Sep. 2019;13(3):483–93. https://doi.org/10.1007/s11708-019-0631-1.
[50] Da Silva M. A Numerical Investigation of Pre-chamber Combustion Engines. King Abdullah University of Science and Technology; 2020.
[51] Eicheldinger S, Wachtmeister G, Nguyen HD, Dinkelacker F. Combustion development for gas engines with extreme BMEPs above 30 bar. MTZ worldwide 2019;80(6):96–103. https://doi.org/10.1007/s38313-019-0034-z.
[52] J. B. Heywood, Internal Combustion Engines Fundamentals. McGraw-Hill, Inc., 1988.
[53] Zeldovich IA, Barenblatt GI, Librovich VB, Makhviladze GM. Mathematical theory of combustion and explosions. Consultants Bureau; 1985.
[54] Williams FA. Combustion Theory Benjamin/Cummings 1985.
[55] F. Accurso, A. Piano, F. Millo, G. Caputo, A. Cimarello, and A. Cafari, Numerical Simulation of a Prechamber-Ignited Lean-Burn Gas Engine by means of Predictive Combustion Models, SAE Int J Engines, vol. 16, no. 5, Dec. 2022, doi: https://doi.org/10.4271/03-16-05-0037.
[56] Guo X, et al. Effects of the nozzle design parameters on turbulent jet development of active pre-chamber. Energy Oct. 2024;306. https://doi.org/10.1016/j.energy.2024.132568.
[57] Liu X, Silva M, Mohan B, AlRamadan AS, Cenker E, Im HG. Computational optimization of the performance of a heavy-duty natural gas pre-chamber engine. Fuel Nov. 2023;352. https://doi.org/10.1016/j.fuel.2023.129075.
[58] Rajasegar R, Niki Y, García-Oliver JM, Li Z, Musculus MPB. Fundamental insights on ignition and combustion of natural gas in an active fueled pre-chamber spark-ignition system. Combust Flame Oct. 2021;232. https://doi.org/10.1016/j.combustflame.2021.111561.
[59] Piano A, Scalambro A, Millo F, Sementa P, Tornatore C, Catapano F. Numerical analysis on the influence of nozzles geometrical features on the combustion process of passive pre-chamber turbulent jet ignition engine. Transp Eng Mar. 2025;19. https://doi.org/10.1016/j.treng.2025.100301.
[60] Shah A, Tunestal P, Johansson B. Effect of pre-chamber volume and nozzle diameter on pre-chamber ignition in heavy duty natural gas engines. In: SAE Technical Papers. SAE International; 2015. https://doi.org/10.4271/2015-01-0867.